Lithospheric Imaging through Reverberant Layers: Sediments, Oceans, and Glaciers

Ziqi Zhang[1] and Tolulope Morayo Olugboji[1]

[1]University of Rochester

November 24, 2022

Abstract

The Earth, in large portions, is covered in oceans, sediments, and glaciers. High-resolution body wave imaging in such environments often suffers from severe reverberations, that is, repeating echoes of the incoming scattered wavefield trapped in the reverberant layer, making interpretation of lithospheric layering difficult. In this study, we propose a systematic data-driven approach, using autocorrelation and homomorphic analysis, to solve the twin problem of detection and elimination of reverberations without a priori knowledge of the elastic structure of the reverberant layers. We demonstrate, using synthetic experiments and data examples, that our approach can effectively identify the signature of reverberations even in cases where the recording seismic array is deployed in complex settings. For example, using data from (1) the Alaska amphibious community seismic experiment (AACSE), (2) Earthscope transportable array stations deployed in the sedimentary basin around the Mississippi embayment, and (3) stations deployed on ice-sediment strata in the glaciers of Antarctica. The elimination of the reverberation is implemented by a frequency domain filter whose parameters are automatically tuned using seismic data alone. Application of our technique to single stations shows that signal enhancement is best when reverberation is attributable to a single layer. On glaciers where the reverberating sediment layer is sandwiched between the lithosphere and an overlying ice layer, homomorphic analysis is preferable in detecting the signature of reverberation. We expect that our technique will see wide application for high-resolution body wave imaging across a wide variety of conditions.

1 # **Lithospheric Imaging through Reverberant Layers:**

2 # **Sediments, Oceans, and Glaciers**

3

4 **Ziqi Zhang[1*]** and Tolulope Olugboji[1]

5 [1] *Department of Earth and Environmental Sciences, University of Rochester, NY*

6

7 Corresponding author: Ziqi Zhang (ziqi.zhang@rochester.edu)

8

9 **Key Points**

10 - A data-driven approach using autocorrelation and homomorphic analysis is
11   proposed to detect the signature of reverberations in seismic data
12 - The proposed approach can be applied to various geological settings where
13   reverberations are present, i.e., sediments, oceans, and glaciers
14 - Signal enhancement is best in single-layer reverberation systems, while homomorphic
15   analysis is preferred for multi-layer systems

16   **Abstract (limit 250 words)**

17   The Earth, in large portions, is covered in oceans, sediments, and glaciers. High-resolution

18   body wave imaging in such environments often suffers from severe reverberations, that is,

19   repeating echoes of the incoming scattered wavefield trapped in the reverberant layer, making

20   interpretation of lithospheric layering difficult. In this study, we propose a systematic data-

21   driven approach, using autocorrelation and homomorphic analysis, to solve the twin problem

22   of detection and elimination of reverberations without a priori knowledge of the elastic

23   structure of the reverberant layers. We demonstrate, using synthetic experiments and data

24   examples, that our approach can effectively identify the signature of reverberations even in

25   cases where the recording seismic array is deployed in complex settings. For example, using

26   data from (1) the Alaska amphibious community seismic experiment (AACSE), (2) Earthscope

27   transportable array stations deployed in the sedimentary basin around the Mississippi

28   embayment, and (3) stations deployed on ice-sediment strata in the glaciers of Antarctica. The

29   elimination of the reverberation is implemented by a frequency domain filter whose

30   parameters are automatically tuned using seismic data alone. Application of our technique to

31   single stations shows that signal enhancement is best when reverberation is attributable to a

32   single layer. On glaciers where the reverberating sediment layer is sandwiched between the

33   lithosphere and an overlying ice layer, homomorphic analysis is preferable in detecting the

34   signature of reverberation. We expect that our technique will see wide application for high-

35   resolution body wave imaging across a wide variety of conditions.

36   **Plain Language Summary (limit 200 words)**

37   The Earth, in large portions, is covered in oceans, sediments, and glaciers. Because of the large

38   structural difference between these layers and the solid Earth underneath, waves get trapped

39   in them which hampers the successful investigation of deeper layers. This is often referred to

40   as "reverberation" or "resonance" - waves that sound or 'sing' again and again. In this study,

41   we propose a systematic approach to detect and eliminate this "singing" effect using only

42   observed data, without any physical knowledge of the local geological structure. Our approach

43   extends the autocorrelation analysis, a widely used method to detect repeating patterns in time

44   series, and also takes advantage of the homomorphic analysis, a popular technique in speech

45   and audio processing. We demonstrate the effectiveness of our approach using both human-

46 generated data and real seismic data, collected from complex geo settings around the world,

47 including in the oceans to the south of the Alaska Peninsula, the Mississippi Embayment, and

48 Antarctica. Application of our approach produces significant signal enhancement in the ocean

49 and sediment environments, where the "singing" effect is simple. We expect that our

50 technique will greatly improve the quality of deep Earth structure investigation across a wide

51 variety of conditions.

52   **1.0 Introduction**

53   The Earth is a water world. As a result, high-resolution body wave imaging of discontinuities

54   across and within its lithospheric shell often involves interpreting data obtained from seismic

55   sensors deployed in the oceans, on the seafloor, or above sediments and glaciers

56   (Anandakrishnan et al., 2000; Clinton et al., 2014; Simon et al., 2021; Suetsugu & Shiobara,

57   2014; Wiens et al., 2021). However, it is well known that in such conditions, the teleseismic

58   body wavefield can be severely contaminated by reverberations (repeating echoes) generated

59   in these shallowest low-velocity layers, i.e., the water column in oceanic environments

60   (Akuhara & Mochizuki, 2015), sediment layer in both continental and oceanic environments

61   (Audet, 2016; Zelt & Ellis, 1999), or the ice layer in the polar regions (Chaput et al., 2014; Cho,

62   2011), therefore, hampering the successful application of high-resolution body wave imaging

63   techniques (Audet, 2016; Chaput et al., 2014; Graw et al., 2017; Janiszewski & Abers, 2015;

64   Kumar et al., 2007). Nevertheless, seismic imaging in these environments is essential to

65   improving our understanding of the dynamics of the Earth. For instance, constraints on the

66   elastic structures of the oceanic plates can shed light on their formation and evolution, and

67   help understand how global plate tectonics operates (Kawakatsu & Utada, 2017; Olugboji et

68   al., 2013; Rychert et al., 2020). Additionally, seismic imaging above thick ice sheets, like

69   Antarctica or Greenland, helps provide constraints on the thermal state, and rheology of the

70   lithosphere, all of which have implications for evolution and stability of glaciers (Blankenship

71   et al., 1993; Fahnestock et al., 2001; W. Shen et al., 2018).

72

73   Many techniques have been developed to accommodate this difficulty of lithospheric imaging

74   in reverberant environments. They include the model-driven wavefield decomposition

75   techniques (Bostock & Tréhu, 2012; Chai et al., 2017; Langston, 2011; Tao et al., 2014), which

76   require a prior knowledge of the seismic structure of the reverberant layer, and data-driven

77   signal processing techniques, which do not require a priori knowledge of the local seismic

78   structures. The latter techniques generally obtain the signature of reverberations from the

79   time-domain autocorrelation of the source-deconvolved seismograms, i.e., receiver functions

80   (Cunningham & Lekic, 2019; Yu et al., 2015), repeating peaks in the frequency-domain power

81   spectra (Zhang & Olugboji, 2021), or from the comparison of synthetic and observed data

82   (Akuhara et al., 2016; Akuhara & Mochizuki, 2015). In all data-driven methods, the physics

83   and signal processing efforts for removing the effect of the reverberation are very similar; it

84 involves designing a resonance removal filter parametrized by the reflection coefficient of the

85 bottom interface trapping the wave and the two-way travel time of the wave in the reverberant

86 layer (Backus, 1959; Yu et al., 2015; Zhang & Olugboji, 2021).

87

88 In choosing when or how to apply a resonance removal filter, a systematic approach to

89 facilitate the detection of the signature and strength of reverberations is needed, so as to ensure

90 more confident and robust signal enhancement. Such an approach should have the ability to

91 handle the complexities and challenges faced when the seismic structure of the reverberant

92 layer varies in a complicated fashion across the array (Barcheck et al., 2020; Laske et al., 2009;

93 Suetsugu et al., 2018). In the most challenging case where reverberations from multiple layers

94 are expressed, i.e., water column, sediments in the oceans, ice sheets and sediments in the

95 polar regions, the existing signal processing methods may fail to disentangle the signature of

96 reverberations due to the complicated nature of the spectra. Therefore, an approach that can

97 effectively detect and characterize the signature of multiple-layer reverberations is required in

98 such scenarios. Taken together, a proposed technique should be automated, or semi-

99 automated, with minimal intervention of the seismic analyst and unaided by a priori elastic

100 properties of the reverberant layers.

101

102 Describing such a method and developing the analytical and associated signal processing tools

103 that show robust utility for lithospheric imaging in reverberant environments is the goal of

104 this work. Our proposed technique is an extension and synthesis of the autocorrelation and

105 homomorphic analysis, with the latter idea borrowing generously from early and recent

106 seismological work in echo detection (Bonner et al., 2002; Buhl et al., 1974; Stoffa et al., 1974)

107 and related ideas in homomorphic speech processing (Bees et al., 1991; Oppenheim & Schafer,

108 2004; Oppenheim, 1969). Homomorphic analysis, while relatively less common in geophysical

109 signal processing, was introduced for source-side echo detection and single-channel source

110 deconvolution (Bonner et al., 2002; Cohen, 1970; Letort et al., 2016). However, unlike classical

111 and modern echo detection, our application here focuses on its use for the detection of

112 repeating, receiver-side echoes, i.e., reverberations.

113

114 Our paper is organized around the two key ideas that are central to our analysis: (1) the

115 automated detection of reverberations, and (2) their elimination using appropriately tuned and

116   robust filter parameters. In the first part on the detection of reverberations, we extend the

117   autocorrelation approach to estimating the presence, strength, and key parameters of the

118   reverberation response. Then, we introduce and apply homomorphic analysis to the refining

119   of the second filter parameter, the echo delay time, especially in the case of a multi-layer

120   reverberation response (i.e., water-sediment and ice-sediment systems). In the second part, we

121   demonstrate the application of the detection and elimination of reverberations using synthetic

122   and real data experiments, showing how our new approach of automatically tuning the

123   resonance removal filters, using seismic data alone, can eliminate the signature of

124   reverberations, even in settings not previously explored. We then discuss how our approach

125   will enable the use of the scattered body wavefield for high-resolution imaging in even more

126   challenging settings around the world.

127

128   **2.0 Method**

129   A seismogram recorded at a station located on or beneath a highly reverberant layer can be

130   seen as a convolution of an earthquake source signal with the impulse response of the receiver-

131   side structures (lithosphere-asthenosphere), and finally the reverberation response of a layer

132   that strongly traps the incoming wave. The strong velocity contrast between the reverberant

133   layer (i.e., water, sediments, and glaciers) and the layer immediately below (i.e., sediment or

134   crust) generates high-amplitude repeating echoes that mask the phases of interest from the

135   crust-mantle boundary or other deeper layers (Figure 1a-b). When the objective is to image

136   the seismic structure beneath the reverberant layer, these trapped waves can be problematic,

137   since they are the strongest signals obscuring any other subsurface conversions and reflections.

138

139   A useful model is to view the reverberations as a generalization of sustained or repeating

140   echoes, that is, waves trapped in a waveguide. The wave transmits into the layer, is reflected

141   perfectly at the top of the layer and is reflected at the bottom repeatedly. In an ideal case, this

142   reverberation response is adequately modeled by a forward resonance filter, which is

143   determined by two parameters: the relative strength of the reverberation, r_0, which is the

144   reflection coefficient at the bottom of the reverberant layer, and the echo delay time, $\tilde{\tau}$, which

145   is the two-way travel time of the waveleg within the reverberant layer. Therefore, a procedure

146   for detection and elimination of the resonance requires identifying these parameters recovered

147   from the seismic signal.

148

149   The first step in reverberation removal is detection. This can be done either by a time-domain

150   autocorrelation analysis or a Fourier-based homomorphic analysis. The autocorrelation

151   technique is simpler and more widely used, so we begin by reviewing its central idea and how

152   it can be extended to detect the presence and strength of the reverberations. In some cases,

153   autocorrelation may fail, due to noisy seismograms or the presence of a hybrid reverberation

154   response (e.g, water-sediment or ice-sediment systems) and can be supplemented by

155   homomorphic analysis. This alternative approach unravels echoes buried in the original signal

156   using a Fourier analysis. It is essential for estimating the echo delay time and has been widely

157   explored in a variety of fields, including audio and speech processing (Deng et al., 2004;

158   Oppenheim, 1969), medical imaging (Wear et al., 1993), and of course, geophysics and

159   seismology (Letort et al., 2018; Scheuer & Wagner, 1985). In our work here, we use it as a

160   supplementary aid to automated echo delay time estimation.

161

162   The signal processing workflow starts with echo detection, then identifying and automatically

163   tuning the reverberation parameters (using both the autocorrelation and homomorphic

164   analysis), and finally ends with resonance removal (Figure 2). If the data does not present

165   strong reverberations, as measured by an echo quality factor, the workflow exits. In this way,

166   the workflow can be used to detect and eliminate reverberations at single station data, or to

167   scan large datasets for signal distortion due to reverberation. In an alternative application, the

168   properties of the reverberating layer, rather than the resonance removal, might be of interest;

169   for example, the goal might be to probe for sediment or ice thickness. In this case, the filter

170   parameters can be used as a set of constraints for estimating the elastic structure of the

171   reverberant layers.

172

173
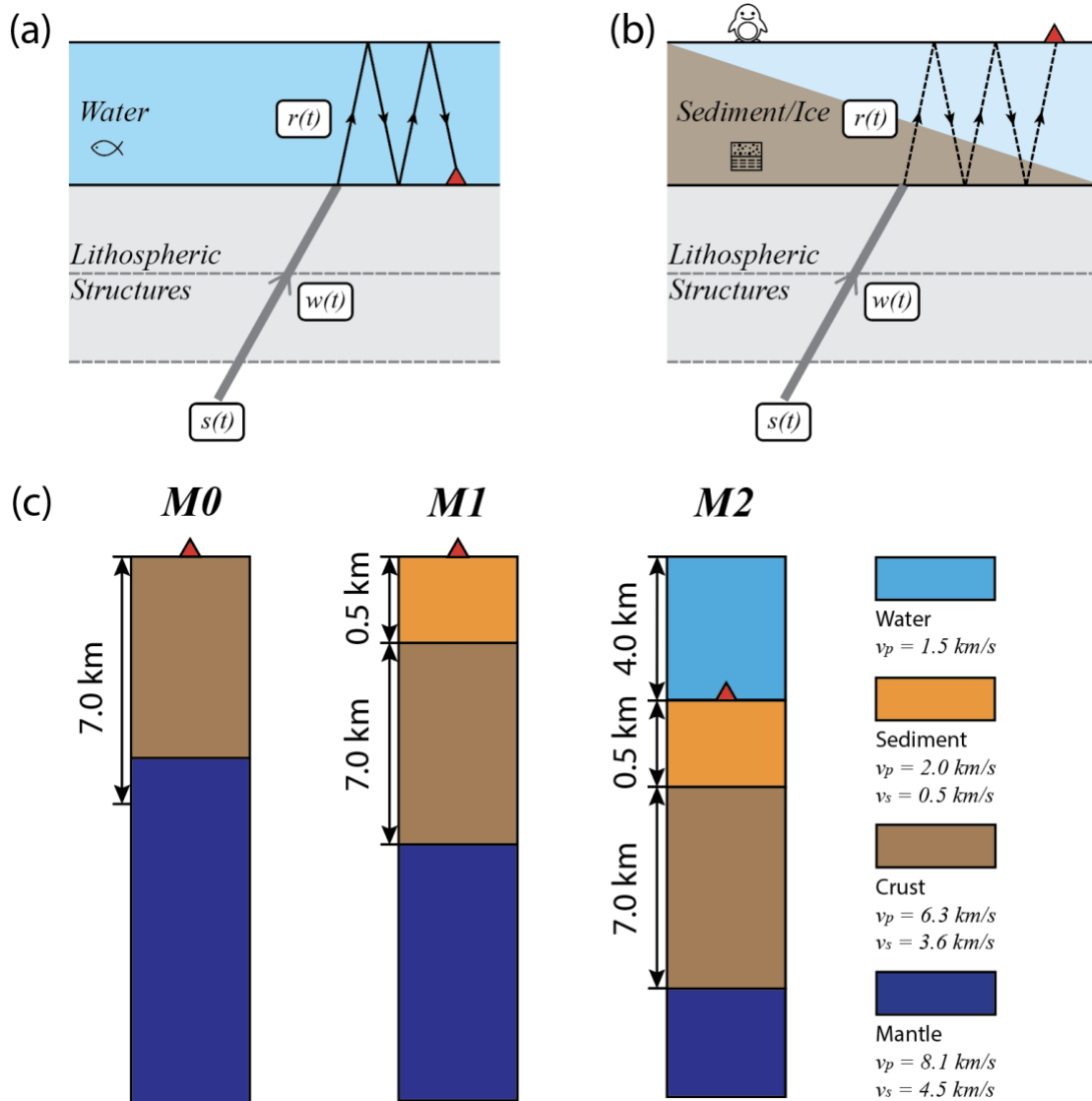
174 **Figure 1**. A schematic diagram illustrating how an incoming teleseismic ray is repeatedly reflected in a reverberant setting: (a)
175 water, (b) sediment and ice. Arrows are P (solid) and S (dashed) waves within the reverberating layers and red triangles
176 represent a seismic recording station. *s(t)* represents the source time function; *w(t)* represents the impulse response of the
177 receiver-side lithospheric structure, i.e., Moho, crustal underplating, or lithosphere-asthenosphere boundary (LAB); *r(t)*
178 represents the reverberation response. In submarine environments, a hybrid situation of water and sediment reverberation
179 may exist. In such a case P-waves are trapped in the water layer above and S-waves are trapped in a sediment layer below.
180 Note that for simplicity we have shown *w(t)* as a continuously transmitting P-wave; in reality, it should be interpreted as
181 representing both transmissions, conversions, and reflections, easily obtained from a reflectivity analysis. (c) Velocity models
182 used in synthetic tests. M0: no reverberation, M1: sediment reverberation, M2: water and sediment reverberations. Red
183 triangles indicate station locations.

184

185
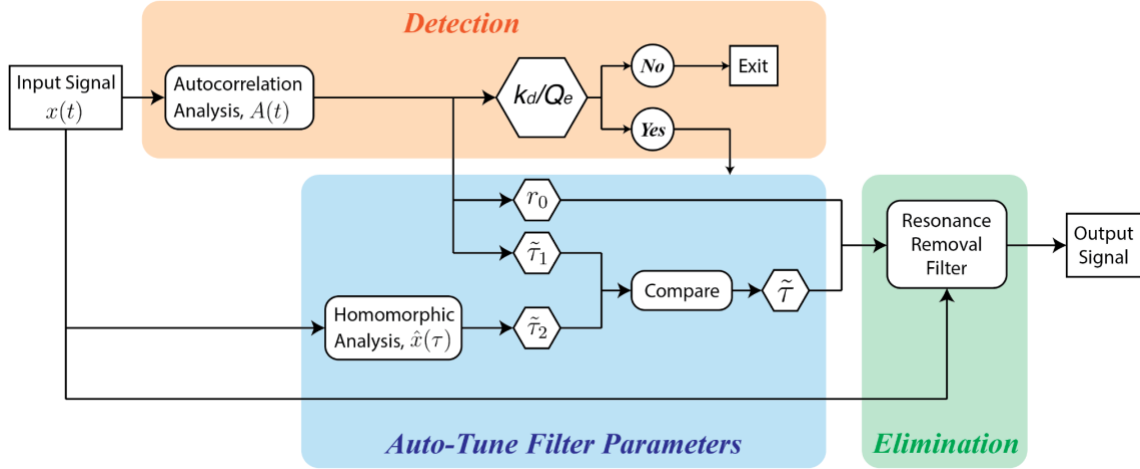
186 **Figure 2**. Signal processing workflow for echo detection and elimination proposed in this study. Detection is obtained from

187 an estimate of the echo number, k_d, and the consequent echo quality factor, Q_e. The response of the reverberating layer,

188 characterized by reverberation strength, r_0, and echo delay time, $\tilde{\tau}$, is auto-tuned using autocorrelation and homomorphic

189 analysis. The resonance removal filter is the inverse of the reverberation response and is applied only when repeating echoes

190 (reverberations) are detected.

191

192 **2.1 Echo Detection with Autocorrelation Analysis**

193 By definition, the autocorrelation function gives the measure of similarity between any signal

194 and its time-delayed version. Therefore, it is easy to see why it is appropriate for detecting the

195 signature of a repeating signal (Phạm & Tkalčić, 2018; Tkalčić et al., 2020). For any input signal

196 $x_0(t)$ that is repeatedly echoed (reverberating), the recorded signal on the seismometer, $x(t)$,

197 and its autocorrelation, $A(t)$, can be written as:

198

$$x(t) = \sum_{n=0}^{\infty} (-r_0)^n x_0(t - n\tilde{\tau})$$

199 (1a)

$$A(t) = \int_{-\infty}^{+\infty} x(t)x(t - \xi)d\xi$$

200 (1b)

201

202 where $\tilde{\tau}$ is the echo delay time, and ξ is the temporal variable in the autocorrelation integral.

203 The autocorrelation of such a reverberant trace should have the form of a decaying sinusoid,

204 showing a large negative peak with amplitude r_0, at the delay time of the first echo: $n = 1$,

205 $A(t = \tilde{\tau})$. Based on this pattern, (Cunningham & Lekic, 2019) showed that fitting a decaying

206   sinusoid curve to the autocorrelation function (hereinafter referred to as fitted autocorrelation,

207   A_f) should result in a robust estimation of the filter parameters:

208

$$A(t) \approx A_f(t) = ce^{-\alpha t}cos\frac{\pi t}{\tilde{\tau}}$$

209   (2)

210   where t is the lag time of the autocorrelation function, $\tilde{\tau}$ is the half-period of the oscillation

211   (which matches the echo delay time of the input signal), c is the autocorrelation amplitude at

212   zero lag time, and α is the damping factor. The filter parameters can now be estimated from

213   the first trough of the fitted autocorrelation curve (Figure 3b). Previous studies have shown

214   that these parameters can be estimated from a priori knowledge of the elastic structure of the

215   reverberant layer, or may be inferred from empirical measurements obtained from seismic

216   data, i.e., power spectra, coherence between vertical and radial components, and

217   autocorrelation (Yu et al., 2015; Zhang & Olugboji, 2021). Here, we utilize the behavior of the

218   autocorrelation function itself (as captured by Equation 2) to detect the presence and strength

219   of repeating echoes in the seismogram.

220

221   The measurement we use here is based on the attenuation response of A_f: the fact that the

222   amplitude of the fitted autocorrelation dies out slowly with strong reverberations and faster

223   with weaker reverberations. We demonstrate this property qualitatively by generating synthetic

224   receiver functions using two different models: with and without a thin sediment layer overlying

225   the crust (models M0 and M1, Figure 1c and Table 1), and calculating the observed and fitted

226   autocorrelation functions (Figure 3). Visually inspecting the results confirms the intuition that

227   the best-fit decaying sinusoid (i.e., the fitted autocorrelation) dies out much more slowly when

228   strong reverberations are present.

229
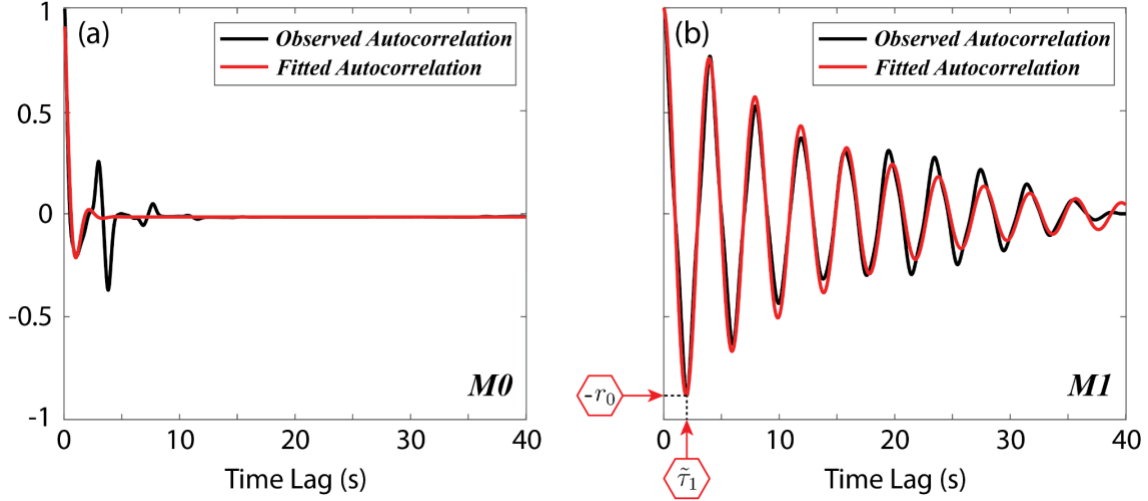
230 **Figure 3.** A comparison between the observed and fitted autocorrelation of a synthetic receiver function with and without

231 the presence of reverberation effect. (a) Observed and fitted autocorrelation curves for the case without reverberation,

232 calculated from the model M0. (b) Observed and fitted autocorrelation curves for the case with reverberation, calculated from

233 model M1. Filter parameters, r_0 and $\tilde{\tau}_1$, are obtained from the first trough of the fitted autocorrelation curve.

234

235 **Table 1**. Density, velocity, and thickness parameters of various layers in the synthetic velocity

236 models.

Layer	Density (kg/m³)	Velocity (km/s)		Velocity Ratio	Thickness, H (km)			
	ρ	v_p	v_s	κ	M0	M1	M2	M3
Ice		4.00	2.00	2.00	-	-	-	2.5
Water	1027	1.50	-	-	-	-	4.0	-
Sediment	2000	2.00	0.50	4.00	-	0.5	0.5	0.5
Crust	2800	6.30	3.60	1.75	7.0	7.0	7.0	7.0
Mantle	3200	8.10	4.50	1.80	-	-	-	-

237

238 To quantify the strength of a reverberation using the property described above, we define an

239 echo number, k_d, which is a measurement of the number of oscillations it takes for the

240 amplitude of the fitted autocorrelation to drop below a level of $e^{-\pi} = 4\%$ of its amplitude at

241 zero time lag. From Equation 2 we can see that

242

243 $$A_{4\%} = A_{t=k_d\tilde{\tau}}$$

244
$$e^{-\pi} = e^{-\alpha k_d \tilde{\tau}} \cos \frac{\pi k_d \tilde{\tau}}{\tilde{\tau}} \longrightarrow k_d = \frac{\pi}{\alpha \tilde{\tau}}$$
(3)

245 A strong reverberation can then be identified by a simple echo quality factor, Q_e, defined using

246 a user-specified threshold of k_{thr}:

247

248 $Q_e = 1$ when $k_d \geq k_{thr}$, indicates strong reverberation (long repeating echoes present)

249 $Q_e = 0$ when $k_d < k_{thr}$, indicates no reverberation (weak or non-repeating echoes)

250

251 We provide a synthetic example to show how k_d and, consequently Q_e, changes when varying

252 the elastic structure of the reverberant sediment layer (Figure 4). We calculate the echo number

253 k_d and the echo quality factor Q_e for a series of synthetic receiver functions generated using a

254 fixed crust and a varying sediment layer. The models used involve increasing the shear velocity

255 and thickness of the sediment layer, such that the echo delay time is fixed at 2.0 s while allowing

256 us to scan the reflection coefficient from 0.8 to 0.2. Note that when the shear velocity and

257 thickness of the sediment reach their highest (3.5 km/s and 3.5 km), the velocity structure of

258 the sediment is almost identical to that of the crust, thus minimizing the reverberation. In this

259 experiment, we see that k_d drops gradually (~22 to 2) as the echo strength (r_0), calculated from

260 the reflection coefficients, decreases from 0.8 to 0.2. Setting the threshold to two echoes, i.e.,

261 $k_{thr} = 2$, results in triggering the echo quality factor on ($Q_e = 1$) if reverberations are detected

262 and off ($Q_e = 0$) otherwise. The seismic analyst can specify a more conservative (i.e., higher)

263 value for k_{thr} if detection is required for the strongest reverberations.
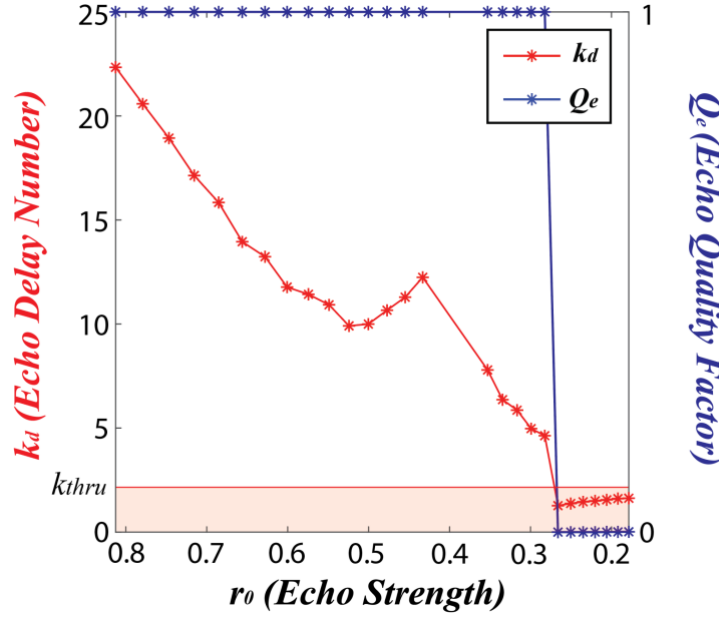
Figure 4. Determining the presence and the strength of reverberation with echo quality factor (Qe). Red and blue curves show relationship between r_0 (reverberation strength) with k_d (echo number) and Qe (echo quality factor), respectively.

2.2 Echo-Delay Time with Homomorphic Analysis

2.2.1 Introduction to Homomorphic Analysis

The treatment of echo detection we just presented is focused on a time-domain representation of the signal. In this presentation, the signature of the repeating echo was successfully obtained from a time-domain measure of similarity of the signal with itself. This is not the only approach for detecting echoes. It turns out that there exists another treatment that makes use of frequency-domain representation of the signals to extract the signature of repeating echoes. This treatment, known as homomorphic analysis, is well documented in classical signal processing (Bogert et al., 1963; Oppenheim & Schafer, 2004) and in early seismology literature as the cepstrum analysis (Stoffa et al., 1974). The key idea is the transformation of signals combined by convolution into new signals combined by addition.

To illustrate the basic principles of homomorphic analysis and the complex cepstrum of any input signal, we reconsider the sampled signal, $x(t)$, which is now composed of a general input wavelet, $x_0(t)$, and a single echo at $\tilde{\tau}$:

$$x(t) = x_0(t) + r_0 x_0(t - \tilde{\tau}) \tag{4a}$$

285     $x(t) = x_0(t) * [\delta(t) + r_0\delta(t - \tilde{\tau})]$ **(4b)**

286

287   where r_0 is the reflection coefficient of the echo and $\delta(t)$ is the Dirac delta function. The

288   signal is now viewed as the convolution of the input wavelet with the echo time series. The

289   Fourier transform of such a signal, $x(t) \xrightarrow{\mathcal{F}} \hat{X}(f)$, is given by

290

291     $X(f) = X_0(f)[1 + r_0 e^{-j2\pi f \tau}]$ **(5)**

292

293   and by taking the logarithm of $X(f)$, we recover a new signal

294

295     $\hat{X}(f) = \log X_0(f) + \log[1 + r_0 e^{-j2\pi f \tau}]$ **(6)**

296

297   In this log-spectrum domain, the echo (second term in Equation 6) is an additive periodic

298   component and the inverse Fourier spectrum, $\hat{X}(f) \xrightarrow{\mathcal{F}^{-1}} \hat{x}(\tau)$, of this transformed signal

299   will exhibit a peak at the echo delay time, $\tilde{\tau}$. The output signal, $\hat{x}(\tau)$, which is the

300   homomorphic transform, $x \xrightarrow{\mathcal{H}} \hat{x}$, is the complex cepstrum of the input signal, $x(t)$, and is,

301   by definition, the inverse Fourier transform of the complex logarithm of the Fourier

302   transformed input signal (Bogert et al., 1963; Childers et al., 1977; Oppenheim, 1969). Note

303   that the output can be viewed as being transformed 'back' into a pseudo-time domain, which

304   is called the "quefrency".

305

306   **2.2.2 Homomorphic Analysis with Synthetic MTC RF**

307   In the extension of homomorphic transform to the general case of a reverberated receiver

308   function trace, $w(t)$, the convolutional model holds:

$$x(t) = w(t) * r(t) = w(t) * \sum_{n=0}^{\infty}(-r_0)^n\delta(t - n\tilde{\tau})$$

309   **(7)**

310   where r_0 and $\tilde{\tau}$ are the reflection coefficient and delay time, respectively. It has previously been

311   shown (Stoffa et al., 1974) that the complex cepstrum of the impulse response of a reverberant

312   layer $r \xrightarrow{\mathcal{H}} \hat{r}$, is given by:

313
$$\hat{r}(\tau) = \sum_{m=1}^{\infty} (-1)^m \frac{(r_0)^m}{m} \delta(\tau - m\tilde{\tau})$$
(8)

314 To demonstrate how to identify echoes in a realistic teleseismic waveform using homomorphic

315 analysis, we present a simple example with a simulated radial receiver function, $w_r(t)$. We first

316 generate an artificial radial seismogram, $x_r(t)$, via spike convolution, that is, by summing time-

317 shifted copies of the vertical seismogram, $x_v(t)$, recorded at GSN station PET from an M6.2

318 earthquake near New Ireland on September 6, 1993 (Figure 5a-b):

319

320
$$x_r(t) = x_v(t) * w(t) * r(t)$$
(9)

321 where

322
$$w(t) = 1.0\delta(t) - 0.8\delta(t-5) + 0.7\delta(t-6) - 0.3\delta(t-7)$$
(10)

323

324 and $r(t)$ is the impulse response of a reverberant layer specified using ten echoes ($n = 10$), a

325 reflection coefficient of $r_0 = 0.6$, and an echo delay time of $\tilde{\tau} = 2.0$ s. The radial receiver

326 function, $w_r(t)$, is then calculated using the MTC (multi-taper correlation) algorithm (Park &

327 Levin, 2000; 2016) (Figure 5c). The complex cepstrum is then estimated by homomorphic

328 transform: $w \xrightarrow{\mathcal{H}} \hat{w}$. Buried in the power cepstrum of $\hat{w}$ is the reverberation response, $\hat{r}$,

329 visible as spectral peaks.

330

331 For clearer identification of these peaks, a high-pass filter (i.e., linear filtering on the log

332 spectrum) is applied to $\hat{w}$, in order to whiten its spectrum and amplify the resonance response.

333 Despite the unique source spectrum in the vertical seismogram, the complex cepstrum of the

334 echoed receiver function, $\hat{w}$, clearly shows a negative peak at 2.0 s ($\tilde{\tau}$) and a positive peak with

335 a lower amplitude at 4.0 s ($2\tilde{\tau}$), which indicates the successful detection of the reverberation

336 response (Figure 5d).

337

338 To accurately determine the echo delay time ($\tilde{\tau}$) from the complex cepstrum, $\hat{w}$, we apply a

339 linear stack with Gaussian smoothing windows at different time intervals:

340
$$S(\tau) = \sum_i \sum_j \gamma_j G(j\tau_i) \hat{w}_r(\tau)$$
(11)

341 where j is the number of delay times (i.e., peaks in the complex cepstrum trace) used in the

342 stack, γ_j is the corresponding weighting factors, $G(j\tau_i)$ is the jth window centered at the ith

343 delay time, and $\hat{w}$ is the complex cepstrum of the receiver function trace.

344

345 In our implementation, we use the first three peaks (i.e., j=1, 2, 3) and set the weighting

346 factors, γ_j, to -0.6, 0.3, -0.1, respectively. The theoretical resonance quefrencies calculated

347 from the two-way travel time match the first few peaks and troughs of the cepstrum curve

348 (dashed lines in Figure 5d). Note that the absolute amplitudes of the peaks and troughs in the

349 power cepstrum gradually decay as quefrency grows. Since the cepstral peaks are already clearly

350 visible at a 2.0 s interval, there is no surprise that the stack, $S(\tau)$, is maximum at echo-delay

351 time $\tilde{\tau}$ = 2.0 s (Figure 5e).

352
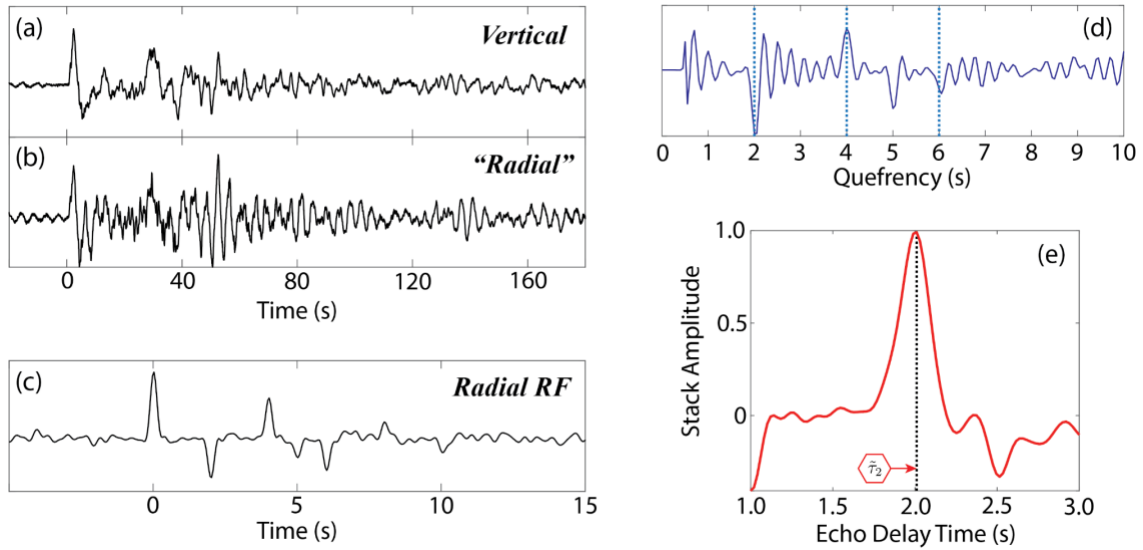
353 **Figure 5**. Homomorphic Analysis with MTC (Multi-Taper Correlation) receiver functions. (a) Vertical seismogram recorded

354 at GSN station PET from an M6.2 earthquake near New Ireland on September 6, 1993. (b) Artificial radial seismogram

355 generated by convolving the vertical record with the prescribed spike series and the echo impulse response, and adding the

356 additive noise. (c) MTC (multi-taper correlations) RF (receiver functions) from reverberated radial seismograms shown in

357 Figure 5b. (d) Complex cepstrum of reverberated RFs shown in Figure 5c. (e) Delay time stack of the reverberated RF

358 cepstrum shown in Figure 5d.

359

360

361 **2.2.3 Homomorphic Analysis with Synthetic RFs**

362 We carry out a similar analysis using synthetic RFs generated with realistic layered models

363 consisting of water and sediment reverberations using the reflectivity technique. In the single-

364 layer case where the reverberation is generated solely from a sediment layer (M1, Figures 1c

365   and Figure 6a), the echo delay time of ~ 2.0 s is clearly detected in the complex cepstrum (i.e.,

366    $\tilde{\tau} = 2.0$ s, $2\tilde{\tau} = 4.0$ s, $3\tilde{\tau} = 6.0$ s, Figure 6b). Consequently, the stack, $S(\tau)$, for echo delay

367   time gives an accurate result of 2.0 s (Figure 6c). In the hybrid case, in which the reverberations

368   are generated from both a water column and a sediment layer (M2, Figures 1c & 6d), two sets

369   of repeating cepstrum peaks can be observed, corresponding to reverberations from sediment

370   and water, respectively ($\tilde{\tau}_s = 2.0$ s and $\tilde{\tau}_w = 5.3$ s, Figure 6e). Since the echo delay times are

371   distinct, applying the stack with two different search windows (1.0 s to 3.0 s for sediment and

372   4.0 s to 6.0 s for water) recovers both echo delay times (Figure 6f-g). In additional tests with

373   noise added to the RF traces, the cepstral traces are noisier and while the signature echoes are

374   harder to visually identify, they can still be estimated by $S(\tau)$ (see Figure S1 in supporting

375   information). In cases where the goal is to recover the signature of more than one reverberant

376   layer, the homomorphic analysis is the preferred approach so long as the echo-delay times of

377   the layers are well separated.

378
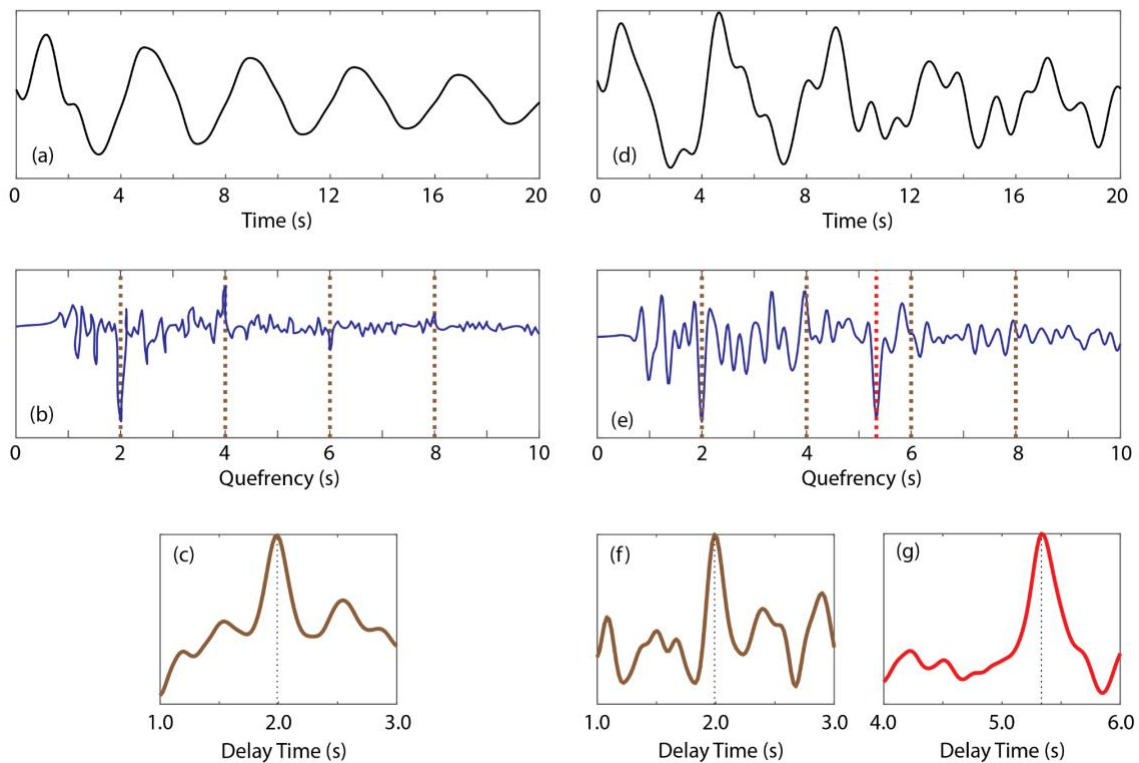
379   **Figure 6**. Homomorphic analysis of synthetic receiver function calculated from (a-c) models M1 and (d-g) M2. (a) Synthetic

380   RF from model M1. (b) Complex cepstrum of the synthetic RF shown in Figure 6a. Brown dashed lines indicate the sediment

381   echo delay time. (c) Delay time stack for complex cepstrum shown in Figure 6b. (d) Synthetic RF from model M2. (e) Complex

382   cepstrum of the synthetic RF shown in Figure 6d. Brown dashed lines and the red dashed line indicate the sediment and water

383   echo delay times, respectively. Note that only the first negative peak of the water echo delay time is visible because of the

384   quefrency axis limit. (f-g) Delay time stack for sediment and water reverberations using the complex cepstrum shown in

385   Figure 6e, respectively.

386

387   **2.3 Frequency Domain Resonance Removal Filter**

388   After the signature of the reverberations has been determined using the described

389   autocorrelation and homomorphic analysis, it can hen be removed from the contaminated

390   signal by building a resonance removal filter in the frequency domain:

391

392   $$F(f) = 1 + r_0 e^{-i2\pi f\tilde{\tau}}$$ (12)

393

394   where r_0 and $\tilde{\tau}$ are the estimated reverberation strength and echo delay time, respectively.

395   Note that $\tilde{\tau}$ is the same two-way travel time of a reflected wave in a trapped layer and with the

396   right substitution, gives the well known equation for the resonance frequency:

397

398   $$f_k = \frac{(2k-1)}{2\tilde{\tau}} \quad \text{where} \quad \tilde{\tau} = 2\frac{d_l}{v_l}$$ (13)

399

400   where d_l and v_l are the thickness and velocity of the reverberant layer. However, in this case,

401   we do not need to know the elastic structure of the reverberant layer, since the echo delay

402   time, $\tilde{\tau}$, is obtained from time-domain autocorrelation, homomorphic analysis, or both (Figure

403   2). We refer the readers to (Zhang & Olugboji, 2021) for a more comprehensive discussion

404   on the design and robustness of the filter. Here, we note that both parameters are reliably

405   recovered by the seismic data alone, without need for a model.

406

407   **3.0 Applications to Seismic Data on Sediments and Oceans**

408   We demonstrate, using both single station and seismic array data, that our proposed workflow

409   can effectively identify the presence of reverberations in the teleseismic body-wave signals.

410

411   **3.1 Single Station Detection and Removal: Sediments (NE68)**

412   We choose a station located in the Songliao basin, northeast China (NE68), which has been

413   previously studied by (Yu et al., 2015). We obtain 195 teleseismic events with magnitudes

414   larger than Mw 6.0, located 30 to 90 degrees away from station NE68, and calculate the

415   receiver function (RF) traces using the MTC (multi-taper correlation) approach, using a cutoff

416   frequency of 1.0 Hz (Figure 7a). The autocorrelation analysis shows strong similarity between

417   the observed and fitted autocorrelation curves at the first few oscillations, and gives an echo

418   number, k_d = 9.83, and consequently an echo quality factor of Q_e= 1 (Figure 7b). Based on

419   the discussion in section 2.1, we determine that sediment reverberation is present in the

420   calculated RFs. We then calculate the complex cepstrum of the RFs and use it to estimate the

421   stack, $S(\tau)$ (Figure 7c-d). The reverberation responses (r_0 = 0.69; $\tilde{\tau}_1$ = 1.31 s and $\tilde{\tau}_2$ = 1.33 s,

422    $\tilde{\tau}$ = 1.32 s) are obtained from the autocorrelation and homomorphic analysis of the receiver

423   function signal. The frequency-domain resonance removal filter, designed using these

424   parameters, is then applied to the original RFs to generate the filtered RFs (Figure 7e).

425

426   After deconvolution of the reverberation response, the direct Ps conversion from the Moho

427   (the first red vertical line) is clearly visible at around 5.0 s compared to the original RFs, in

428   which the conversion phase is completely buried in the reverberations (Figure 7a). Note that

429   the amplitudes of the following multiples (the second and third red vertical lines) are relatively

430   small due to the high amplitude of the PbS phase (i.e., Ps conversion at the sediment-crust

431   boundary) at around 1.0 s in the filtered RF (Figure 7e). Nevertheless, the $H - \kappa$ stacking

432   (using a crustal P velocity of 6.4 km/s (Tao et al., 2014) can still take advantage of the moveout

433   information and gives a clear result. Our obtained crustal thickness (35.0 km) and P-to-S

434   velocity ratio (1.73) are consistent with those obtained by (Yu et al., 2015), who reported a

435   crustal thickness of 35.2 km and a P-to-S velocity ratio of 1.74.
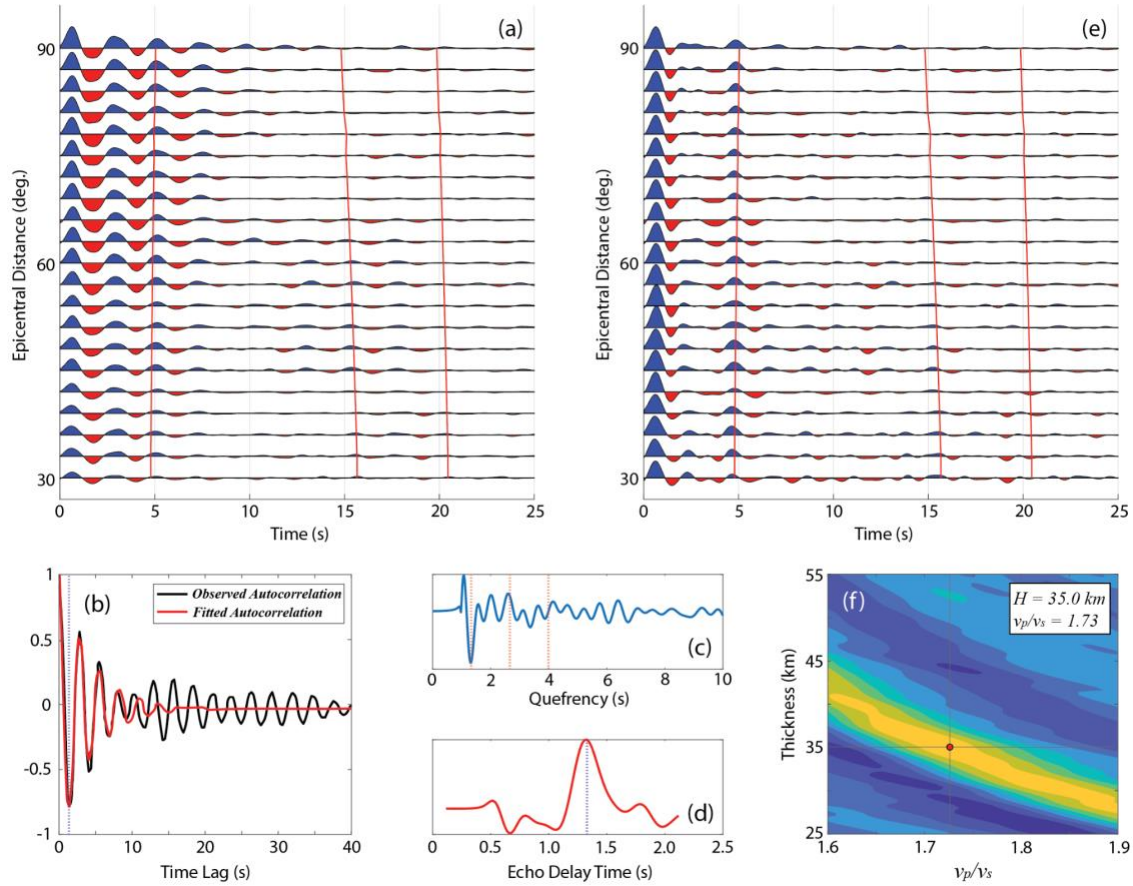
Figure 7. Application of the echo detection and elimination workflow to teleseismic data recorded at station NE68. (a) Original RFs plotted against epicentral distance. Red vertical lines indicate the estimated arrival times for Ps conversion at the Moho and its multiples. (b) Observed and fitted autocorrelation functions. The blue dashed line indicates the echo delay time determined from the autocorrelation analysis. (c) Complex cepstrum of the original RFs. (d) Delay time stack of the complex cepstrum. The blue dashed line indicates the echo delay time determined from the homomorphic analysis. (e) Filtered RFs plotted against epicentral distance. (f) $H - \kappa$ stacking using the filtered RFs.

3.2 Echo Detection on Sedimentary Basins: The Upper Mississippi Embayment

The second example we turn to is the Earthscope transportable array around the Upper Mississippi Embayment, located near the New Madrid seismic zone (Figure 8). Again, this is a region whose crustal structure has previously been investigated by (Liu et al., 2017) using receiver function and gravity constraints. In their investigation, they applied resonance removal filters to some of the stations, to obtain more reliable reflectivity images, however, it was unclear why the stations were chosen. In this case study, we apply the detection module of our FADER workflow (Figure 2) to receiver functions calculated from teleseismic data recorded at 31 stations of the Transportable Array (TA) of the USArray project in the study area, to determine the presence and strength of the sediment reverberations. The calculated

453 echo number, k_d, ranges from 1.08 to 9.10 across the region, with most of the stations

454 expressing the strongest reverberations located inside the Upper Mississippi Embayment,

455 particularly to the east of the study area. We are able to match, with accuracy, all stations where

456 (Liu et al., 2017) detects reverberations. However, we also observe some stations to the west

457 of the UME with notable reverberations, which may benefit from a reconsideration in future

458 imaging efforts (see Table S1 in supporting information for a compilation of the reverberation

459 response).
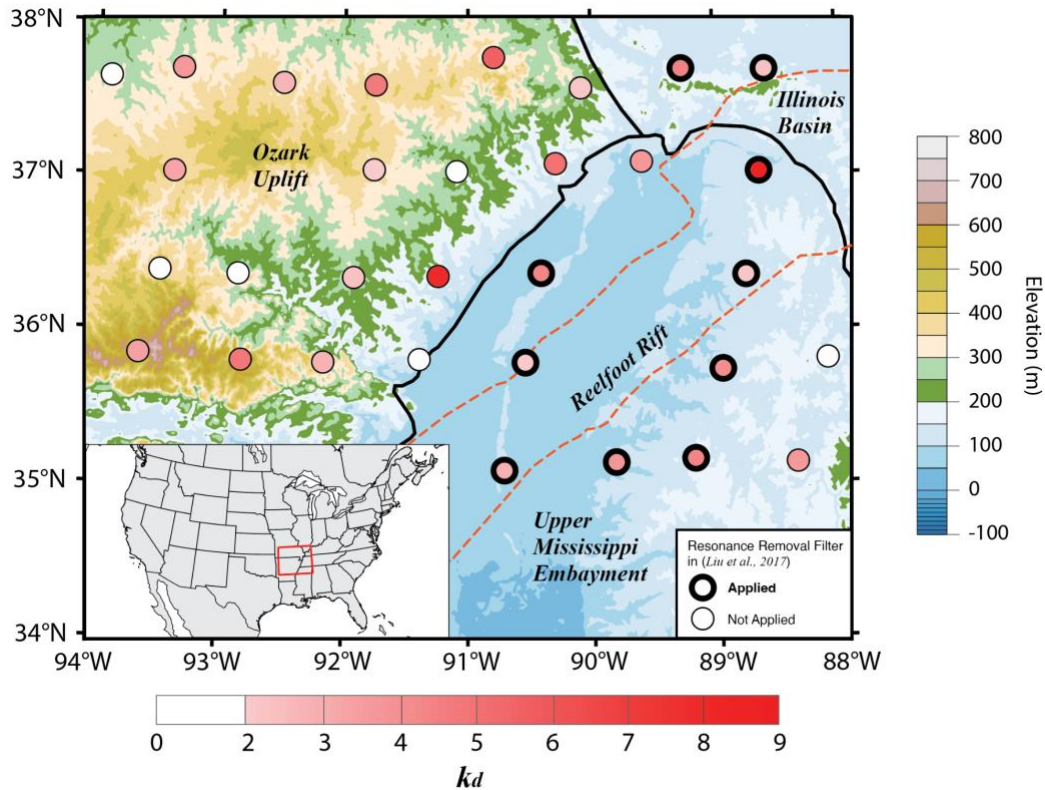
460

461 **Figure 8**. Echo detection in and around the Upper Mississippi Embayment. Major tectonic features are shown in black lines;

462 the location of the Reelfoot Rift is marked in orange dashed lines. Stations expressing strong reverberation, as detected by

463 (Liu et al., 2017), are identified by thick boundaries (thin line otherwise); the color of the circles indicates k_d values obtained

464 in this study.

465 **3.3 Echo Detection on a Submarine Array: The Alaska Experiment**

466 A third example is taken from another seismic array, but one located in the oceans and not on

467 land (model M2 of Figure 1c). This is a seismic array crossing from deep oceans into shallow

468 oceans, deployed across the subducting pacific plate. The Alaska Amphibious Community

469   Seismic Experiment (AACSE) presents a unique opportunity to conduct high-resolution

470   seismic imaging of the lithosphere-asthenosphere system of the Pacific plate, prior to

471   subduction (Barcheck et al., 2020). This is only possible if the reverberation response can be

472   modeled successfully. We obtain teleseismic data, and calculate receiver functions, using data

473   from fifty ocean bottom seismometers (OBS) of the AACSE array. The echo number, k_d,

474   obtained from autocorrelation analysis, ranges from 0.78 to 13.04, across the array. An echo

475   threshold, $k_{thr} = 2$, suggests that reverberations exist at over half of the stations (Figure 9). A

476   comparison of the measured echo delay times, with predicted water reverberations, at stations

477   expressing the strongest reverberations, suggests that the reverberations are from the sediment

478   layer underneath the stations and not from the water-layer above (see Figure S2 in supporting

479   information). This is a promising evaluation because it allows the straightforward

480   deconvolution of the reverberation response, following careful estimation of the relevant

481   parameters of a single sediment layer.

482
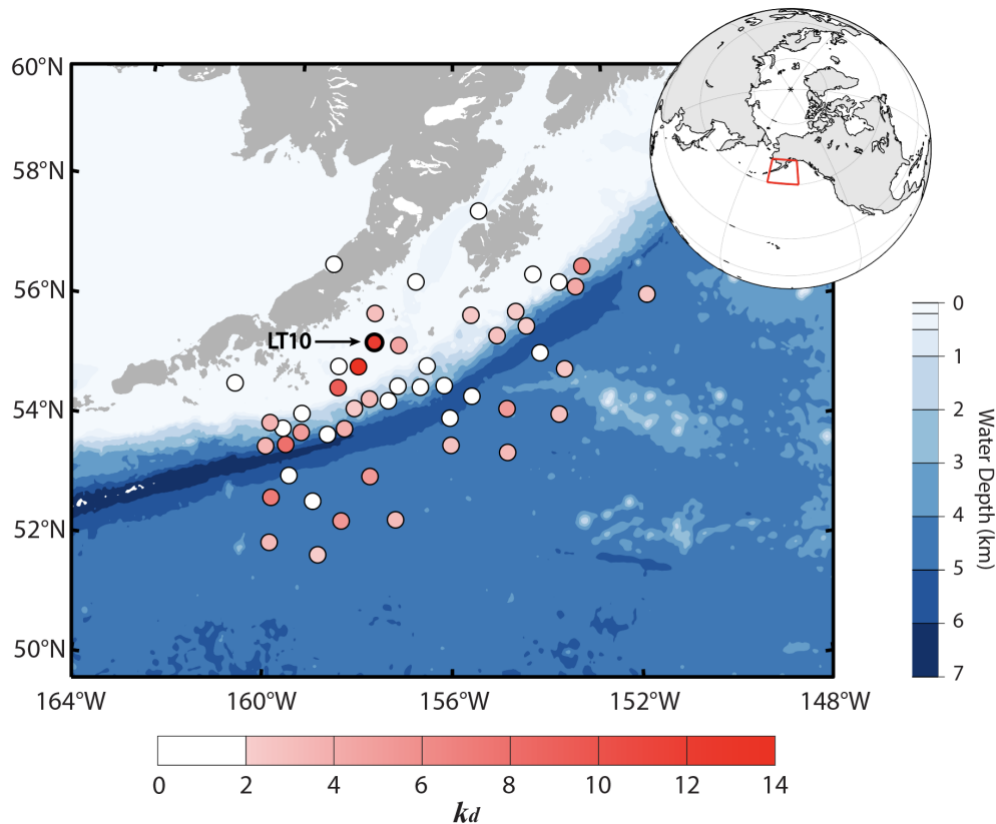
483   **Figure 9**. Echo detection in the Aleutian subduction zone. Circles denote OBS locations and the color of the circles indicates

484   k_d values. Station LT10 is highlighted for further analysis in Figure 10.

485

486   Here we present an example demonstrating the detection and elimination of reverberations

487   for one of the most reverberant stations on AACSE (LT10). We obtain 115 teleseismic events

488   with magnitudes larger than Mw 6.0, located 30 to 90 degrees away from the station, and

489   calculate the receiver function (RF) traces using the MTC (multi-taper correlation) approach,

490   using a cutoff frequency of 1.0 Hz (Figure 10a). Using autocorrelation and homomorphic

491   analysis, we determine an echo delay time of $\tilde{\tau} = 1.63$ s and a reverberation strength of $r_0 =$

492   0.47 (Figure 10b-d). After resonance removal, the coherence of later-arriving phases are

493   improved in the filtered RFs, with clear detection of lithospheric conversions and their

494   multiples significantly enhanced. For example, a strong and clear arrival at ~ 3 s (Figure 10e)

495   is observed. The $H - \kappa$ stacking using an average P velocity of 6.3 km/s (Eberhart-Phillips

496   & Christensen, 2006) gives a layer thickness of 19.4 km/s and a velocity ratio of 1.76 (Figure

497   10f). We interpret this to be the boundary of the middle crust and an ultramafic-mafic lower

498   crust, as previously detected by wide angle active source imaging (Shillington et al., 2004). The

499   signature of this layer had previously been obscured and illustrates why interpretations of the

500   teleseismic body-wavefield should be treated with caution when the possibility of distortions

501   from reverberations are not accounted for.
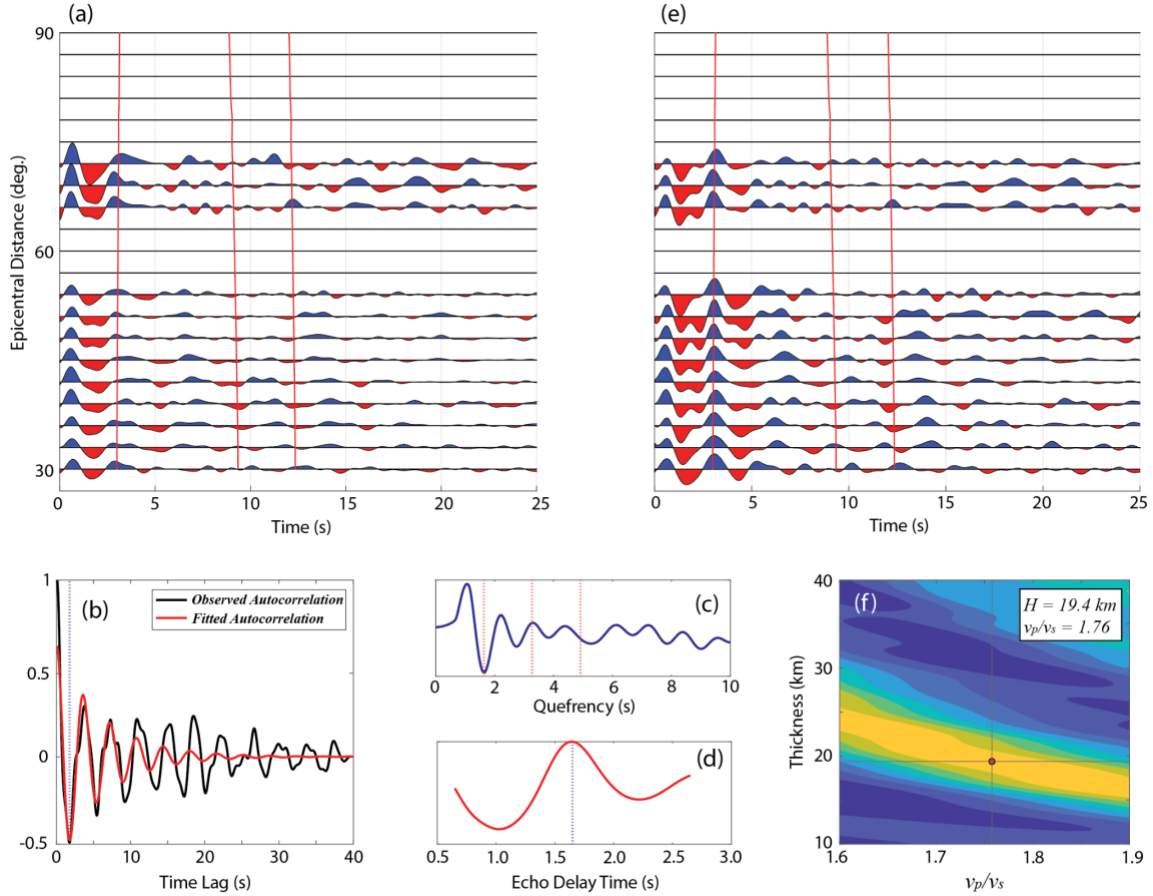
Figure 10. Application of the echo detection and elimination workflow to teleseismic data recorded at station LT10 located in the Aleutian subduction zone. (a) Original RFs plotted against epicentral distance. Some epicentral distance bins do not have RF traces due to the lack of events. Red vertical lines indicate the estimated arrival times for Ps conversion at the interface detected and its multiples. (b) Observed and fitted autocorrelation functions. The blue dashed line indicates the echo delay time determined from the autocorrelation analysis. (c) Complex cepstrum of the original RFs shown in Figure 10a. (d) Delay time stack of the complex cepstrum. The blue dashed line indicates the echo delay time determined from the homomorphic analysis. (e) Filtered RFs plotted against epicentral distance. (f) $H - \kappa$ stacking using the filtered RFs.

4.0 Echo Detection When Both Ice and Sediment is Present

We now turn to a more complicated setting where reverberations are generated from both an ice layer and a sedimentary layer. Although similar, at first sight, to the previous example, one major difference between the water-sediment and the ice-sediment response is that in the former case, for submarine deployments, the station is sandwiched between the two layers (model M2, Figure 1c), while in the latter case it is located on top of the two layers: ice-sediment (model M3, Figure 11a). In the water-sediment system, reverberations from the two layers are distinct and decoupled, arriving separately at the station, enabling the homomorphic analysis to detect two distinct echo delay times (Figure 6e-g). In the ice-sediment system,

520   however, the station is on top of the ice layer, and the reverberations are now mixed, expressed

521   as a sum (in the homomorphic signal) of the combined effects of the ice and the sediment

522   layers.

523

524   We demonstrate this using synthetic RFs generated for layered model M3, which consists of

525   both ice and sediment layers (Figure 11a). In this model, the two-way travel times (i.e., echo

526   delay times) within the ice and sediment layers are $\tilde{\tau}_i$ = 2.5 s and $\tilde{\tau}_s$ = 2.0 s (calculated from

527   Equation 13). The reverberation response of the ice and sediment layers (as a hybrid

528   reverberant layer) is obtained from homomorphic analysis as a sum of the two echo delay

529   times, that is $\tilde{\tau}_i+\tilde{\tau}_s$ = 4.5 s. We can see from the RF traces that the conversion phases

530   associated with the sediment-crust interface have the largest amplitudes, while the Ps

531   conversion at the Moho shows much lower amplitudes and its multiples are hardly visible

532   (Figure 11b).

533

534   In this scenario, the autocorrelation analysis shows strong reverberation behavior with an echo

535   number of k_d = 34.43 (Figure 11c), however, the estimated echo delay time of 1.47 s does not

536   match any of the individual layer values ($\tilde{\tau}_i$, $\tilde{\tau}_s$, or $\tilde{\tau}_i+\tilde{\tau}_s$). The complex cepstrum, however,

537   shows clear repeating negative and positive peaks (Figure 11d), indicating the presence of

538   strong echoes in the data. A stack for the relevant echo-delay time gives a strong detection at

539   4.5 s (Figure 11e). This value matches that of the sum for both the ice and sediment layers. In

540   the synthetic RF traces, the strong sediment phases at ~ 4.0 s are clearly repeated multiple

541   times, separated by this interval (arrows in Figure 11b), visually confirming detection

542   parameters of the homomorphic analysis.

543

544   To make these discoveries concrete, we apply the homomorphic analysis to teleseismic data

545   collected from 18 stations deployed on the Antarctica glacier (Figure 12a). We obtain the echo

546   delay times at each station from the stack of complex cepstrums of the receiver functions, and

547   compare them with predicted ice-only echo delay times calculated using ice thicknesses

548   obtained from the analysis of seismic data presented by (Phạm & Tkalčić, 2018). Their results

549   are obtained from autocorrelation of radial and vertical seismograms, to extract the single-

550   layer ice response. Our obtained echo delay times generally agree with those calculated from

551   results from (Phạm & Tkalčić, 2018), with an average difference of 11.7%. In some cases, we

552   detect longer echo delay times (11 of 18 stations), which possibly indicates reverberations

553   generated not only from the ice sheets, but also from the sedimentary layer beneath (Figure

554   12b).

555
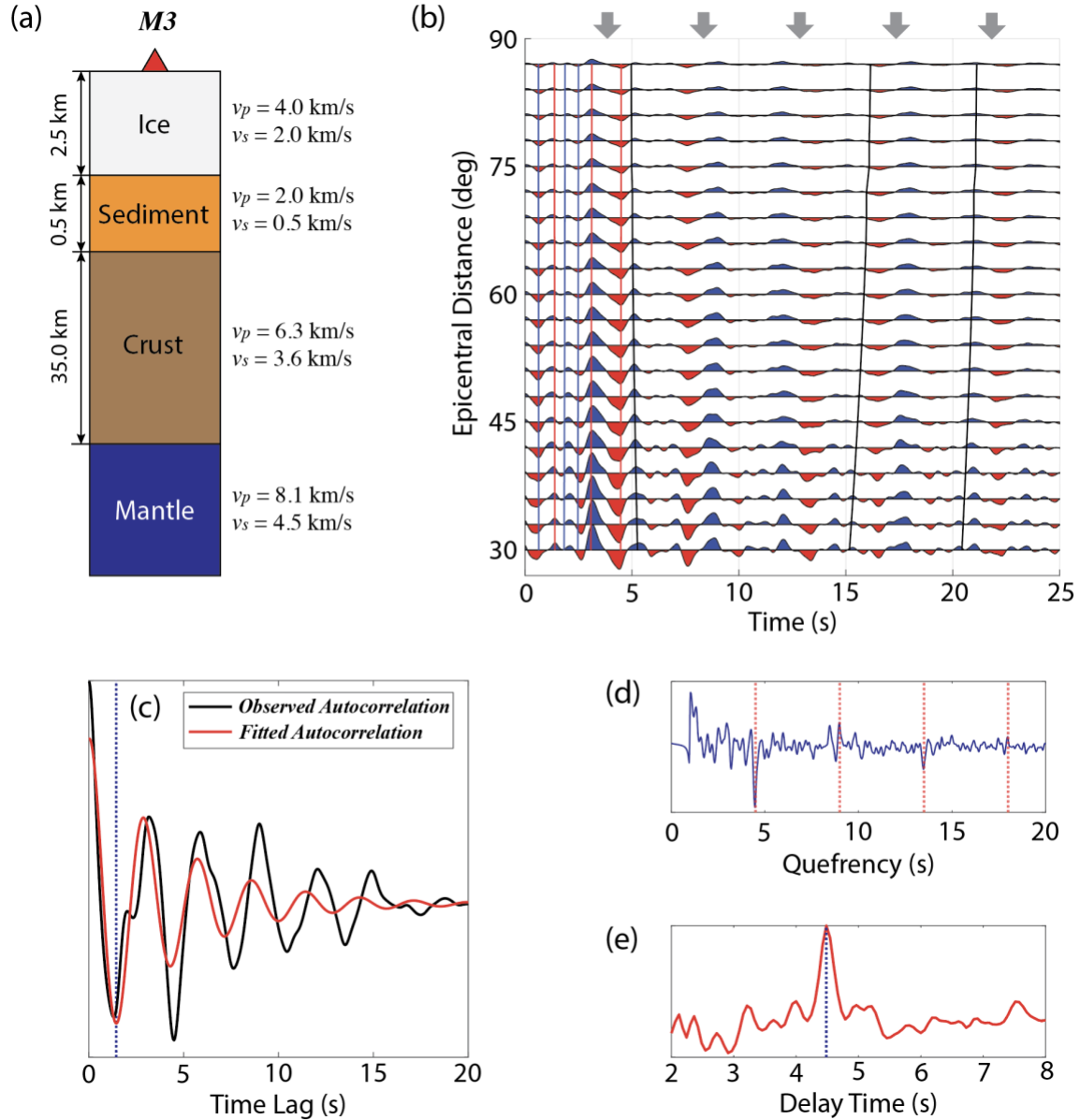
556   **Figure 11.** Synthetic experiment on echo detection when both ice and sediment layer present. (a) Layered model (M3)

557   consisting of an ice layer, a sediment layer, a crustal layer, and a mantle half-space. (b) Synthetic RFs and theoretical arrivals

558   of Ps conversions and their multiples associated with the bottom of ice, sediment, and crust (Blue, red, and black vertical

559   lines, respectively). (c) Observed and fitted autocorrelation curves showing the estimated echo delay time (black dashed line),

560   which does not match the input model. (d) Complex cepstrum and repeating quefrency peaks (red dashed lines) (e) Linear

561   stack for the correct echo delay time (blue dashed line). The observed autocorrelation and the complex cepstrum are

562   computed from the synthetic receiver functions in b. The signature of the repeating echoes detected by homomorphic analysis

563   can be seen as doublets (marked by gray arrow in b).
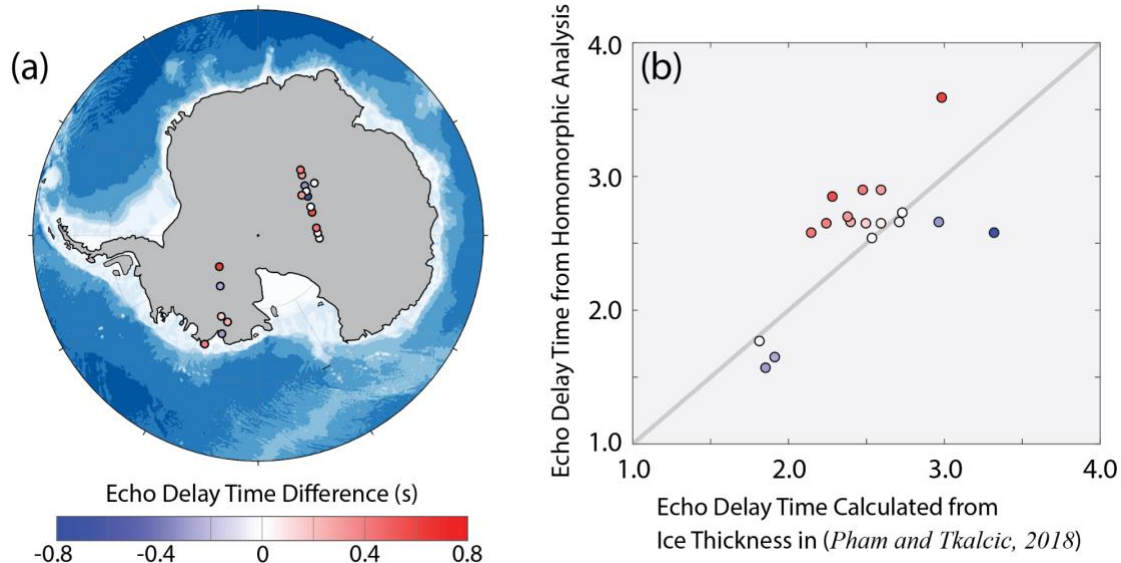
Figure 12. Comparison of echo delay times in Antarctica using homomorphic analysis (this study) with those calculated for ice thicknesses derived from elastic structure estimated by (Phạm & Tkalčić, 2018). (a) Locations of the stations (circles) and the estimated echo delay time difference (filled colors). (b) A comparison of our measured echo delay times (vertical axis) and those for ice (horizontal axis), calculated from (Phạm & Tkalčić, 2018). We refer the readers to Table S3 in supporting information for the detailed results of the absolute echo delay times.

5.0 Discussions

5.1 Fast and Automated Detection and Elimination of Echoes and Reverberations

In this study, we utilized both autocorrelation and homomorphic analysis to detect and eliminate the effect of reverberations from teleseismic body wave signals. We note that although this type of reverberation is but one of many classes of resonant seismic noise (Hellweg, 2000; Roman, 2017), it differs from stationary harmonic noise in that it is signal-generated, time-limited, and methods for removing stationary harmonic noise are not appropriately suited for its elimination (Zali et al., 2021). In order to emphasize the receiver-side reverberation response, we use an input receiver function signal obtained by preprocessing the seismogram through source-deconvolution. In the case when only a single channel sensor is available i.e, acoustic sensors like MERMAID (Pipatprathanporn & Simons, 2021; Simon et al., 2021), other source normalization techniques might be necessary to achieve a similar effect (Bensen et al., 2007; Shen et al., 2012; Tkalčić et al., 2020).

In the single-layer scenario where reverberations are generated solely from a sedimentary layer, or in the decoupled water-sediment system (Figures 7 & 10), an automated workflow can be

587 assembled based on the approach we outlined (Figures 2). The input source-deconvolved

588 signal (i.e., receiver function) is first passed into the autocorrelation analysis to determine the

589 presence and strength of reverberations. With a threshold for the echo number appropriately

590 defined, this process can be performed automatically. An estimate of the parameters of the

591 reverberation response, r_0 and $\tilde{\tau}_1$, is also obtained in this step. If reverberations are detected,

592 the input signal is further analyzed by the homomorphic analysis, where an appropriate search

593 window for the cepstral stack is determined by using $\tilde{\tau}_1 \pm \Delta\tau$. If the output echo delay time

594 from this second step ($\tilde{\tau}_2$) agrees with the previous one ($\tilde{\tau}_1$), an average of the two can be taken

595 as the final echo delay time. If they are off by a prescribed tolerance, the analyst can visually

596 inspect the underlying autocorrelation curves or the complex cepstrum stacks (Figures 3 and

597 5) to judge which of these is more reliable, and decide if further data processing is necessary.

598 The resonance removal filter can then be designed to remove the reverberation response from

599 the input signal, using the estimated filter parameters. In the non-acoustic case where the

600 seismic sensor is on the bottom of the ocean, the water reverberations are negligible due to

601 their longer delay time and the lower transmission onto the radial seismogram (Zhang &

602 Olugboji, 2021).

603

604 In an alternative application only detection and not elimination might be required (i.e., sections

605 3.2 and 3.3). An example is investigating if the reverberations do not affect late arriving

606 conversions where $k_d << t_{Ps}$ from a specific lithospheric discontinuity (underplated crust or

607 mantle layering). The aforementioned workflow can be easily adapted to perform this task,

608 with the input being receiver functions from each station and the output being the echo

609 number (k_d) and the consequent echo quality factor (Q_e), which determines the presence and

610 strength of the reverberations. In this application, the workflow is still automated, and only

611 autocorrelation analysis is used. Since our proposed workflow uses autocorrelation analysis to

612 detect echoes, it may fail when a complicated seismic structure exists, i.e., in ice-sediment

613 systems (see section 4). In this case, we recommend using the homomorphic analysis. When

614 supplemented with a crude estimation of local ice and sediment thickness and shear velocity,

615 if any, it can provide information on how to interpret the signature of the hybrid reverberation

616 response.

617 **5.2 Homomorphic Deconvolution of the Reverberation Response**

618 As we have demonstrated extensively, homomorphic analysis is an effective approach to
619 identifying the signature of echoes in the sampled signals. Since the homomorphic
620 transformation maps convolution into addition, one might expect that a natural extension to
621 removing the reverberation response would be to subtract the cepstral peaks associated with
622 reverberations in the quefrency domain and calculate the inverse complex cepstrum, which
623 recovers the original signal. This is the case known as homomorphic deconvolution. This
624 approach to removing unwanted convolutional components from the time series has already
625 been explored for removing synthetic reverberations and seismic source deconvolution (Stoffa
626 et al., 1974; Ulrych, 1971). However, it has been pointed out that several factors, i.e., low-
627 frequency assumption of the source, compromised estimation in phase unwrapping, and the
628 presence of additive noise, make it unstable for practical applications (Bostock & Sacchi, 1997;
629 Clayton & Wiggins, 1976). Although homomorphic deconvolution is not used for
630 reverberation elimination in this study, we present a synthetic experiment here to demonstrate
631 its principles and shortcomings.

632

633 We generate a signal using a series of spike functions that put peaks and troughs at 1 s, 5 s,
634 and 6 s (Figure 13a). We then convolve this signal with a reverberation series consisting of ten
635 echoes ($n = 10$), with a reflection coefficient of $r_0 = 0.6$ and an echo delay time of $\tilde{\tau} = 1.0$ s
636 (Figure 13b). The complex cepstrum is then calculated by the homomorphic analysis described
637 in section 2.2 (Figure 13c). Cepstral peaks are clearly visible at a 1.0 s quefrency interval, with
638 the first three especially profound. These three peaks are removed from the complex cepstrum
639 trace by setting the amplitudes to the average of their neighboring points (Figure 13d).

640
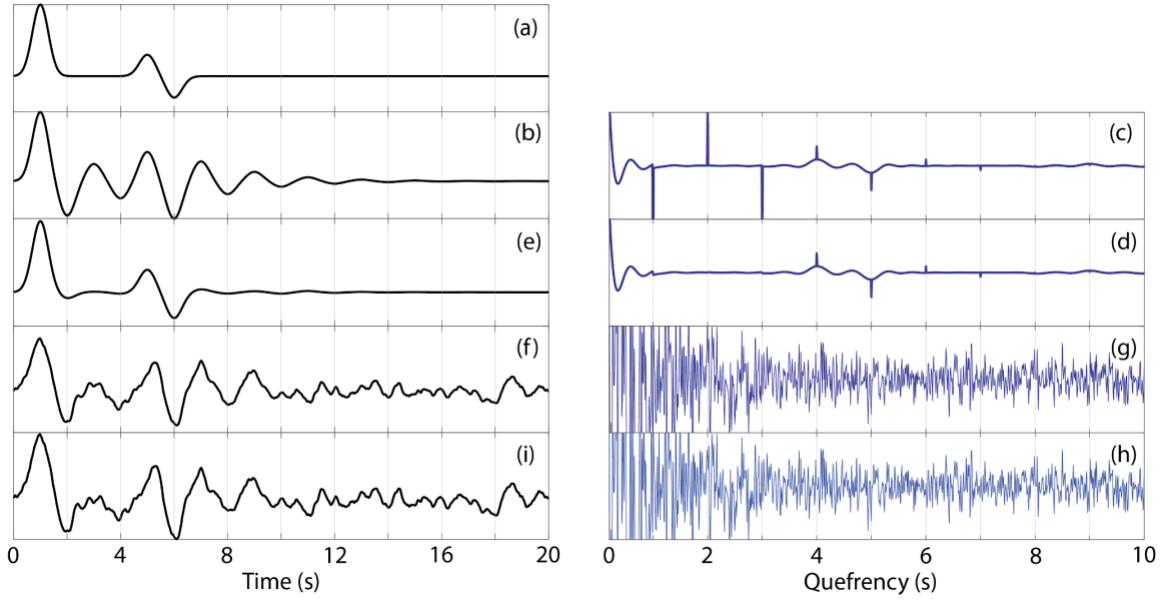
Figure 13. Homomorphic deconvolution with synthetic sampled signals. (a) Reference sampled signal generated by spike functions. (b) Signal in Figure 11a with reverberation. (c) Complex cepstrum of reverberated signal in Figure 11b. (d) Complex cepstrum shown in Figure 11c with the first three cepstral peaks removed. (e) Recovered time-domain signal from the inverse cepstrum transform of the complex transform in Figure 11d. (f) Signal in Figure 11b with additive noise added. (g) Complex cepstrum of reverberated signal in Figure 11f. (h) Complex cepstrum shown in Figure 11g with the first three theoretical cepstral peaks removed. (i) Recovered time-domain signal from the inverse cepstrum transform of the complex transform in Figure 11h.

We then perform an inverse cepstrum transform, which is the complex exponential of the Fourier transform of the complex cepstrum ($\hat{x} \xrightarrow{\mathcal{H}^{-1}} x$). The resulting signal is nearly identical to the reference signal, even though we only remove the first three, but not all the cepstral peaks in the quefrency domain (Figure 13e). However, with strong additive noise added to the sampled signal (Figure 13f), the complex cepstrum shows a much more complicated pattern and the theoretical cepstral peaks, which are supposed to show up at a 1.0 s interval, are hardly visible (Figure 13g). Since the noise is additive, not convolutional, the homomorphic transform cannot separate it from the clean signal spectrum, and thus, result in a very noisy complex cepstrum. With no surprise, averaging the theoretical cepstral peaks results in an almost identical noisy cepstrum trace (Figure 13h) and can no longer recover the original signal with inverse cepstrum transform (Figure 13i).

6.0 Conclusion

663

664 In this study, we have addressed the problem of high-resolution imaging of the crust and

665 mantle lithosphere using the teleseismic body-wavefield that suffers severe distortion from

666 complex scattering through reverberant structures - sediments, oceans and glaciers. We

667 develop an automated technique for identifying the signature and strength of reverberations

668 and to eliminate its negative effect. We do this by extending and applying autocorrelation and

669 homomorphic analysis to detection, and robust filter design, enabling the deconvolution of

670 the reverberation response. We demonstrate, using synthetic experiments, that our approach

671 is effective in a wide variety of scenarios. Real data examples, with seismic arrays in the Upper

672 Mississippi Embayment and the Aleutian subduction zone, shows that detection and

673 elimination of reverberations should be conducted routinely before the interpretation of

674 results for subsurface lithospheric layering. In the more complicated environment of glaciers,

675 where both ice and sediment are present, homomorphic analysis is preferred. We anticipate

676 application of our workflow across a variety of seismic deployments where the reverberation

677 challenge has limited the utility of teleseismic body wave data for lithospheric imaging.

678

679 **7.0 Data Availability Statement**

680

681 All seismic data used in this study can be obtained from the IRIS Data management center

682 (https://ds.iris.edu/ds) under the network codes YP (station NE68), TA (Earthscope

683 transportable array stations in the UME), XO (the Alaska amphibious community seismic

684 experiment, AACSE), YT and ZM (Antarctica). Synthetic receiver functions were computed

685 using the Telewavesim open-source python library provided by (Audet et al., 2019). The

686 receiver function deconvolution was computed using compiled C++ code provided by

687 (Olugboji & Park, 2016). The MatLab code for fitting a decaying sinusoid can be retrieved

688 from (Amberg, 2022). The MatLab package of the proposed workflow for Fast and

689 Automated Detection and Elimination of Echoes and Reverberations (FADER) can be

690 retrieved from (Zhang & Olugboji, 2022).

691 **8.0 Acknowledgements**

References Cited

Akuhara, T., & Mochizuki, K. (2015). Hydrous state of the subducting Philippine Sea plate inferred from receiver function image using onshore and offshore data. *Journal of Geophysical Research, [Solid Earth]*, *120*(12), 8461–8477. https://doi.org/10.1002/2015JB012336

Akuhara, T., Mochizuki, K., Kawakatsu, H., & Takeuchi, N. (2016). Non-linear waveform analysis for water-layer response and its application to high-frequency receiver function analysis using OBS array. *Geophysical Journal International*, *206*(3), 1914–1920. https://doi.org/10.1093/gji/ggw253

Amberg, D. (2022). *Fit a damped sine wave* [MATLAB Central File Exchange]. Retrieved from https://www.mathworks.com/matlabcentral/fileexchange/50756-fit-a-damped-sine-wave

Anandakrishnan, S., Voigt, D. E., Burkett, P. G., Long, B., & Henry, R. (2000). Deployment of a broadband seismic network in west Antarctica. *Geophysical Research Letters*, *27*(14), 2053–2056. https://doi.org/10.1029/1999gl011189

Audet, P. (2016). Receiver functions using OBS data: promises and limitations from numerical modelling and examples from the Cascadia Initiative. *Geophysical Journal International*, *205*(3), 1740–1755. https://doi.org/10.1093/gji/ggw111

Audet, P., Thomson, C., Bostock, M., & Eulenfeld, T. (2019). Telewavesim: Python software for teleseismic body wave modeling. *Journal of Open Source Software*, *4*(44), 1818. https://doi.org/10.21105/joss.01818

Backus, M. M. (1959). WATER REVERBERATIONS—THEIR NATURE AND ELIMINATION. *Geophysics*, *24*(2), 233–261. https://doi.org/10.1190/1.1438579

Barcheck, G., Abers, G. A., Adams, A. N., Bécel, A., Collins, J., Gaherty, J. B., et al. (2020). The Alaska Amphibious Community Seismic Experiment. *Bulletin of the Seismological Society of America*, *91*(6), 3054–3063. Retrieved from https://pubs.geoscienceworld.org/ssa/srl/article-pdf/91/6/3054/5176819/srl-2020189.1.pdf

Bees, Blostein, & Kabal. (1991). Reverberant speech enhancement using cepstral processing. In *Acoustics, Speech, and Signal Processing, IEEE International Conference on* (Vol. 0, pp. 977–980). computer.org. https://doi.org/10.1109/ICASSP.1991.150504

Bensen, G. D., Ritzwoller, M. H., Barmin, M. P., Levshin, a. L., Lin, F., Moschetti, M. P., et al. (2007). Processing seismic ambient noise data to obtain reliable broad-band surface wave dispersion measurements. *Geophysical Journal International*, *169*(3), 1239–1260. https://doi.org/10.1111/j.1365-246X.2007.03374.x

Blankenship, D. D., Bell, R. E., Hodge, S. M., Brozena, J. M., Behrendt, J. C., & Finn, C. A. (1993). Active volcanism beneath the West Antarctic ice sheet and implications for ice-sheet stability. *Nature*, *361*(6412), 526–529. https://doi.org/10.1038/361526a0

Bogert, B. P., Healy, M. J. R., & Tukey, J. W. (1963). The quefrency alanysis of time series for echoes ; Cepstrum, pseudo-autocovariance, cross-cepstrum and saphe cracking. *Time Series Analysis*, 209–243. Retrieved from https://ci.nii.ac.jp/naid/10006519906/

Bonner, J. L., Reiter, D. T., & Shumway, R. H. (2002). Application of a Cepstral F Statistic for Improved Depth Estimation. *Bulletin of the Seismological Society of America*, *92*(5), 1675–1693. https://doi.org/10.1785/0120010128

Bostock, M. G., & Sacchi, M. D. (1997). Deconvolution of teleseismic recordings for mantle structure. *Geophysical Journal International*, *129*(1), 143–152. https://doi.org/10.1111/j.1365-246X.1997.tb00943.x

Bostock, M. G., & Tréhu, A. M. (2012). Wave-Field Decomposition of Ocean Bottom Seismograms. *Bulletin of the Seismological Society of America*, *102*(4), 1681–1692. https://doi.org/10.1785/0120110162

Buhl, P., Stoffa, P. L., & Bryan, G. M. (1974). The application of homomorphic deconvolution to Shallow-Water marine seismology—part ii: Real data. *Geophysics*, *39*(4), 417–426. https://doi.org/10.1190/1.1440439

Chai, C., Ammon, C. J., Anandakrishnan, S., Ramirez, C., & Nyblade, A. (2017). Estimating subglacial structure using P-

739   wave receiver functions. *Geophysical Journal International*, *209*(2), 1064–1079. https://doi.org/10.1093/gji/ggx075

740   Chaput, J., Aster, R. C., Huerta, A., Sun, X., Lloyd, A., Wiens, D., et al. (2014). The crustal thickness of West Antarctica.

741   *Journal of Geophysical Research, [Solid Earth]*, *119*(1), 378–395. https://doi.org/10.1002/2013jb010642

742   Childers, D. G., Skinner, D. P., & Kemerait, R. C. (1977). The cepstrum: A guide to processing. *Proceedings of the IEEE*,

743   *65*(10), 1428–1443. https://doi.org/10.1109/PROC.1977.10747

744   Cho, T. (2011). Removing Reverberation in Ice Sheets from Receiver Functions. *Seismological Research Letters*, *82*(2), 207–210.

745   https://doi.org/10.1785/gssrl.82.2.207

746   Clayton, R. W., & Wiggins, R. A. (1976). Source shape estimation and deconvolution of teleseismic bodywaves. *Geophysical*

747   *Journal International*, *47*(1), 151–177. https://doi.org/10.1111/j.1365-246X.1976.tb01267.x

748   Clinton, J. F., Nettles, M., Walter, F., Anderson, K., Dahl-Jensen, T., Giardini, D., et al. (2014). Seismic network in

749   Greenland monitors earth and ice system. *Eos*, *95*(2), 13–14. https://doi.org/10.1002/2014eo020001

750   Cohen, T. J. (1970). Source-Depth Determinations using Spectral, Pseudo-Autocorrelation and Cepstral Analysis. *Geophysical*

751   *Journal International*, *20*(2), 223–231. https://doi.org/10.1111/j.1365-246X.1970.tb06065.x

752   Cunningham, E., & Lekic, V. (2019). Constraining crustal structure in the presence of sediment: a multiple converted wave

753   approach. *Geophysical Journal International*, *219*(1), 313–327. https://doi.org/10.1093/gji/ggz298

754   Deng, L., Droppo, J., & Acero, A. (2004). Estimating cepstrum of speech under the presence of noise using a joint prior of

755   static and dynamic features. *IEEE Transactions on Audio, Speech, and Language Processing*, *12*(3), 218–233.

756   https://doi.org/10.1109/TSA.2003.822627

757   Eberhart-Phillips, D., & Christensen, D. H. (2006). Imaging the transition from Aleutian subduction to Yakutat collision in

758   central Alaska, with local earthquakes and active source data. *Journal of*. https://doi.org/10.1029/2005JB004240

759   Fahnestock, M., Abdalati, W., Joughin, I., Brozena, J., & Gogineni, P. (2001). High Geothermal Heat Flow, Basal Melt, and

760   the Origin of Rapid Ice Flow in Central Greenland. *Science*, *294*(5550), 2338–2342.

761   https://doi.org/10.1126/science.1065370

762   Graw, J. H., Hansen, S. E., Langston, C. A., Young, B. A., Mostafanejad, A., & Park, Y. (2017). An Assessment of Crustal

763   and Upper-Mantle Velocity Structure by Removing the Effect of an Ice Layer on the P-Wave Response: An

764   Application to Antarctic Seismic Studies. *Bulletin of the Seismological Society of America*, *107*(2), 639–651. Retrieved from

765   https://pubs.geoscienceworld.org/ssa/bssa/article-abstract/107/2/639/354175

766   Hellweg, M. (2000). Physical models for the source of Lascar's harmonic tremor. *Journal of Volcanology and Geothermal Research*,

767   *101*(1), 183–198. https://doi.org/10.1016/S0377-0273(00)00163-3

768   Janiszewski, H. A., & Abers, G. A. (2015). Imaging the Plate Interface in the Cascadia Seismogenic Zone: New Constraints

769   from Offshore Receiver Functions. *Seismological Research Letters*, *86*(5), 1261–1269.

770   https://doi.org/10.1785/0220150104

771   Kawakatsu, H., & Utada, H. (2017). Seismic and Electrical Signatures of the Lithosphere–Asthenosphere System of the

772   Normal Oceanic Mantle. *Annual Review of Earth and Planetary Sciences*, *45*(1), 139–167.

773   https://doi.org/10.1146/annurev-earth-063016-020319

774   Kumar, P., Kind, R., Priestley, K., & Dahl-Jensen, T. (2007). Crustal structure of Iceland and Greenland from receiver

775   function studies. *Journal of Geophysical Research*, *112*(B3). https://doi.org/10.1029/2005jb003991

776   Langston, C. A. (2011). Wave-field continuation and decomposition for passive seismic imaging under deep unconsolidated

777   sediments. *Bulletin of the Seismological Society of America*, *101*(5), 2176–2190. https://doi.org/10.1785/0120100299

778   Laske, G., Collins, J. A., & Wolfe, C. J. (2009). Probing the Hawaiian hot spot with new broadband ocean bottom

779   instruments. *Eos, Transactions, American Geophysical Union* . Retrieved from

780   https://agupubs.onlinelibrary.wiley.com/doi/abs/10.1029/2009EO410002

781 Letort, J., Bollinger, L., Lyon-Caen, H., Guilhem, A., Cano, Y., Baillard, C., & Adhikari, L. B. (2016). Teleseismic depth
782   estimation of the 2015 Gorkha−Nepal aftershocks. *Geophysical Journal International*, *207*(3), 1584–1595.
783   https://doi.org/10.1093/gji/ggw364

784 Letort, J., Trilla, A. G., Ford, S. R., & Myers, S. C. (2018). Multiobjective Optimization of Regional and Teleseismic Data to
785   Constrain the Source of the 12 September 2016 M w 5.4 Earthquake in South Korea. *Bulletin of the Seismological Society of*
786   *America*, *108*(1), 175–187. Retrieved from https://pubs.geoscienceworld.org/ssa/bssa/article-
787   abstract/108/1/175/524870

788 Liu, L., Gao, S. S., Liu, K. H., & Mickus, K. (2017). Receiver function and gravity constraints on crustal structure and
789   vertical movements of the Upper Mississippi Embayment and Ozark Uplift. *Journal of Geophysical Research, [Solid Earth]*,
790   *122*(6), 4572–4583. https://doi.org/10.1002/2017jb014201

791 Olugboji, T. M., & Park, J. (2016). Crustal anisotropy beneath Pacific Ocean-Islands from harmonic decomposition of
792   receiver functions. *Geochemistry, Geophysics, Geosystems*, *17*(3), 810–832. https://doi.org/10.1002/2015GC006166

793 Olugboji, T. M., Karato, S.-I., & Park, J. (2013). Structures of the oceanic lithosphere-asthenosphere boundary: Mineral-
794   physics modeling and seismological signatures. *Geochemistry, Geophysics, Geosystems*, *14*(4), 880–901. Retrieved from
795   https://agupubs.onlinelibrary.wiley.com/doi/abs/10.1002/ggge.20086

796 Oppenheim, A. V. (1969). Speech analysis-synthesis system based on homomorphic filtering. *The Journal of the Acoustical*
797   *Society of America*, *45*(2), 458–465. https://doi.org/10.1121/1.1911395

798 Oppenheim, A. V., & Schafer, R. W. (2004). From frequency to quefrency: A history of the cepstrum. *IEEE Signal Processing*
799   *Magazine*, *21*(5), 95–106. Retrieved from https://ieeexplore.ieee.org/abstract/document/1328092/

800 Park, J., & Levin, V. (2000). Receiver functions from multiple-taper spectral correlation Estimates. *Bulletin of the Seismological*
801   *Society of America*, *90*(6), 1507–1520. https://doi.org/10.1785/0119990122

802 Park, J., & Levin, V. (2016). Statistics and frequency-domain moveout for multiple-taper receiver functions. *Geophysical*
803   *Journal International*, *207*(1), 512–527. https://doi.org/10.1093/gji/ggw291

804 Phạm, T.-S., & Tkalčić, H. (2018). Antarctic ice properties revealed from teleseismic P wave coda autocorrelation. *Journal of*
805   *Geophysical Research, [Solid Earth]*, *123*(9), 7896–7912. https://doi.org/10.1029/2018jb016115

806 Pipatprathanporn, S., & Simons, F. J. (2021). One year of sound recorded by a mermaid float in the Pacific: hydroacoustic
807   earthquake signals and infrasonic ambient noise. *Geophysical Journal International*, *228*(1), 193–212.
808   https://doi.org/10.1093/gji/ggab296

809 Roman, D. C. (2017). Automated detection and characterization of harmonic tremor in continuous seismic data. *Geophysical*
810   *Research Letters*, *44*(12), 6065–6073. https://doi.org/10.1002/2017gl073715

811 Rychert, C., Harmon, N., Constable, S., & Wang, S. (2020). The nature of the Lithosphere‐Asthenosphere Boundary. *Journal*
812   *of Geophysical Research, [Solid Earth]*. https://doi.org/10.1029/2018JB016463

813 Scheuer, T. E., & Wagner, D. E. (1985). Deconvolution by autocepstral windowing. *Geophysics*, *50*(10), 1533–1540.
814   https://doi.org/10.1190/1.1441843

815 Shen, W., Wiens, D. A., Anandakrishnan, S., Aster, R. C., Gerstoft, P., Bromirski, P. D., et al. (2018). The crust and upper
816   mantle structure of central and west Antarctica from Bayesian inversion of Rayleigh wave and receiver functions.
817   *Journal of Geophysical Research, [Solid Earth]*, *123*(9), 7824–7849. https://doi.org/10.1029/2017jb015346

818 Shen, Y., Ren, Y., Gao, H., & Savage, B. (2012). An improved method to extract very-broadband empirical green's
819   functions from ambient seismic noise. *Bulletin of the Seismological Society of America*, *102*(4), 1872–1877.
820   https://doi.org/10.1785/0120120023

821 Shillington, D. J., Van Avendonk, H. J. A., Holbrook, W. S., Kelemen, P. B., & Hornbach, M. J. (2004). Composition and
822   structure of the central Aleutian island arc from arc-parallel wide-angle seismic data. *Geochemistry, Geophysics, Geosystems*,

823   *5*(10). https://doi.org/10.1029/2004gc000715

824   Simon, J. D., Simons, F. J., & Irving, J. C. E. (2021). Recording earthquakes for tomographic imaging of the mantle beneath

825   the South Pacific by autonomous MERMAID floats. *Geophysical Journal International*, *228*(1), 147–170.

826   https://doi.org/10.1093/gji/ggab271

827   Stoffa, P. L., Buhl, P., & Bryan, G. M. (1974). THE APPLICATION OF HOMOMORPHIC DECONVOLUTION TO

828   SHALLOW-WATER MARINE SEISMOLOGY—PART I: MODELS. *Geophysics*, *39*(4), 401–416.

829   https://doi.org/10.1190/1.1440438

830   Suetsugu, D., & Shiobara, H. (2014). Broadband Ocean-Bottom Seismology. *Annual Review of Earth and Planetary Sciences*,

831   *42*(1), 27–43. https://doi.org/10.1146/annurev-earth-060313-054818

832   Suetsugu, D., Shiobara, H., Sugioka, H., Tada, N., Ito, A., Isse, T., et al. (2018). The OJP array: seismological and

833   electromagnetic observation on seafloor and islands in the Ontong Java Plateau. *JAMSTEC Report of Research and*

834   *Development*, *26*, 54–64. https://doi.org/10.5918/jamstecr.26.54

835   Tao, K., Liu, T., Ning, J., & Niu, F. (2014). Estimating sedimentary and crustal structure using wavefield continuation:

836   theory, techniques and applications. *Geophysical Journal International*, *197*(1), 443–457.

837   https://doi.org/10.1093/gji/ggt515

838   Tkalčić, H., Phạm, T.-S., & Wang, S. (2020). The Earth's coda correlation wavefield: Rise of the new paradigm and recent

839   advances. *Earth-Science Reviews*, *208*, 103285. https://doi.org/10.1016/j.earscirev.2020.103285

840   Ulrych, T. J. (1971). Application of homomorphic deconvolution to seismology. *Geophysics*, *36*(4), 650–660.

841   https://doi.org/10.1190/1.1440202

842   Wear, K. A., Wagner, R. F., Insana, M. F., & Hall, T. J. (1993). Application of autoregressive spectral analysis to cepstral

843   estimation of mean scatterer spacing. *IEEE Transactions on Ultrasonics, Ferroelectrics, and Frequency Control*, *40*(1), 50–58.

844   https://doi.org/10.1109/58.184998

845   Wiens, D. A., Shen, W., & Lloyd, A. J. (2021). The seismic structure of the Antarctic upper mantle. *Geological Society, London,*

846   *Memoirs*, *56*. https://doi.org/10.1144/M56-2020-18

847   Yu, Y., Song, J., Liu, K. H., & Gao, S. S. (2015). Determining crustal structure beneath seismic stations overlying a low-

848   velocity sedimentary layer using receiver functions: RECEIVER FUNCTION CRUSTAL STUDY. *Journal of*

849   *Geophysical Research, [Solid Earth]*, *120*(5), 3208–3218. https://doi.org/10.1002/2014JB011610

850   Zali, Z., Ohrnberger, M., Scherbaum, F., Cotton, F., & Eibl, E. P. S. (2021). Volcanic Tremor Extraction and Earthquake

851   Detection Using Music Information Retrieval Algorithms. *Seismological Research Letters*, *92*(6).

852   https://doi.org/10.1785/0220210016

853   Zelt, B. C., & Ellis, R. M. (1999). Receiver-function studies in the Trans-Hudson Orogen, Saskatchewan. *Canadian Journal of*

854   *Earth Sciences*, *36*(4), 585–603. https://doi.org/10.1139/e98-109

855   Zhang, Z., & Olugboji, T. (2021). The signature and elimination of sediment reverberations on submarine receiver

856   functions. *Journal of Geophysical Research, [Solid Earth]*, *126*(5). https://doi.org/10.1029/2020jb021567

857   Zhang, Z., & Olugboji, T. (2022). *URseismology/FADER: v0.1.0*. https://doi.org/10.5281/zenodo.6804873